

# Dynamic Contrast Enhanced Magnetic Resonance Imaging in Oncology: Theory, Data Acquisition, Analysis, and Examples

Thomas E. Yankeelov<sup>1-4\*</sup> and John C. Gore<sup>1-5</sup>

<sup>1</sup>Institute of Imaging Science, Departments of <sup>2</sup>Radiology and Radiological Sciences, <sup>3</sup>Physics and Astronomy, <sup>4</sup>Biomedical Engineering, <sup>5</sup>Molecular Physiology and Biophysics, USA

**Abstract:** Dynamic contrast enhanced MRI (DCE-MRI) enables the quantitative assessment of tumor status and has found application in both pre-clinical tumor models as well as clinical oncology. DCE-MRI requires the serial acquisition of images before and after the injection of a paramagnetic contrast agent so that the variation of MR signal intensity with time can be recorded for each image voxel. As the agent enters into a tissue, it changes the MR signal intensity from the tissue to a degree that depends on the local concentration. After the agent is transported out of the tissue, the MR signal intensity returns to its baseline value. By analyzing the associated signal intensity time course using an appropriate mathematical model, physiological parameters related to blood flow, vessel permeability, and tissue volume fractions can be extracted for each voxel or region of interest.

In this review we first discuss the basic physics of this methodology, and then present technical aspects of how DCE-MRI data are acquired and analyzed. We also discuss appropriate models of contrast agent kinetics and how these can be used to elucidate tissue characteristics of importance in cancer biology. We conclude by briefly summarizing some future goals and demands of DCE-MRI.

**Keywords:** DCE-MRI, pharmacokinetics, cancer, compartmental modeling, contrast agent.

## 1. INTRODUCTION

When a malignant tumor reaches a few mm<sup>3</sup> in volume, it can no longer rely on the passive diffusion of metabolites from host tissue blood vessels to be able to continue to proliferate, so new vasculature must develop in order for the tumor to continue to thrive [1,2]. This process of neovascularization or angiogenesis [3] is a signature of neoplasms and one of the principal potential targets for quantitative imaging [4]. It is believed that virtually all solid tumors are dependent upon angiogenesis for survival [5], and many anti-angiogenic drugs are currently in clinical trials [6]. Thus, methods for imaging and quantitatively assessing this phenomenon will be useful in clinical oncology.

In contrast to mature blood vessels that are the result of normal physiologic processes, tumor vessels produced by angiogenesis are characteristically leaky, fragile, and incompletely formed [1-3]. These differences may be exploited in order to characterize the neovasculature and, indirectly, the state of the tumor. Dynamic contrast enhanced magnetic resonance imaging (DCE-MRI) is an imaging technique that can measure the density, integrity and leakiness of tissue vasculature. Changes in the parameters obtained by DCE-MRI can be used to assess longitudinal changes within a tumor and, in particular, how a tumor is responding to treatment. The method is based on measurements and mathematical models of how a tracer perfuses through such vessels. Healthy vessels in normal tissues may be characterized by a range of parameters measuring blood flow, vessel permeability, and tissue volume fractions (i.e., fractions of a given sample of tissue that can be attributed to

intravascular or extravascular space). It is a plausible hypothesis that some or all of these parameters will be different in pathologic vessels. In recent years, there has been great interest and considerable development in the use of DCE-MRI to study these phenomena and test this hypothesis.

Magnetic resonance imaging (MRI) is a versatile radiological imaging modality that is widely used in clinical practice for the diagnosis and evaluation of a broad range of disorders, including cancer [7,8]. MRI can non-invasively, and without the hazard of ionizing radiation, produce high resolution images in multiple (arbitrary) planes of the interior of the body. There are several different types of MR images, some of which are exquisitely sensitive to subtle changes within soft tissues. MRI uses magnetic fields and radiofrequency energy to acquire signals (that are then used to construct images) from mobile hydrogen nuclei, contained mainly in tissue water. The contrast depicted in MR images is typically due to variations from tissue to tissue in the density of hydrogen nuclei, and/or in other MR properties such as the relaxation times  $T_1$  and  $T_2$ , which largely depend on the macromolecular composition of tissues. The intrinsic contrast between soft tissues and many pathologies is sufficiently great that often contrast agents are not needed or used with MRI. Nonetheless, appropriate exogenous contrast agents have been developed for use with MRI and are safely used in many clinical imaging procedures [9].

MRI contrast agents (CAs) are pharmaceuticals administered to a subject during the imaging procedure that are designed to increase the contrast between different tissues. CAs alter the MR signals from tissues by changing a tissue's inherent proton density and/or the relaxation rates. Except for spaces that can be filled (such as the stomach and gastrointestinal tract) there are few opportunities for significantly changing proton density, so most agents in use are designed to alter the relaxation times  $T_1$  and/or  $T_2$  and

\*Address correspondence to this author at the Vanderbilt University Institute of Imaging Science, 1161 21<sup>st</sup> Avenue South, AA 1105 Medical Center North, Nashville, Tennessee 37232-2310, USA; E-mail: thomas.yankeelov@vanderbilt.edu

$T_2^*$ . CAs are sometimes categorized according to the **relative changes** they impart on either  $T_1$  and/or  $T_2$ . A CA that predominantly decreases  $T_1$  is often called a **positive relaxation agent** because the  $T_1$  shortening causes a **signal intensity increase** in some  $T_1$ -weighted images. Conversely, a CA that predominantly reduces  $T_2$  is usually referred to as a negative relaxation agent because the  $T_2$  reduction results in signal intensity decrease in a  $T_2$ -weighted image. This review will consider only the first kind of CA and is organized as follows: We first (briefly) describe the elementary physics involved in magnetic resonance relaxation, followed by a discussion of how contrast agents can affect relaxation times. The basic methods by which dynamic contrast enhanced MRI (DCE-MRI) data are acquired are presented, followed by common methods of analyzing such data. The applications of DCE-MRI acquisition and analysis methods as applied to both pre-clinical and clinical studies are then explored. We conclude by looking to the future of DCE-MRI.

## 2. BASIC PHYSICS OF MAGNETIC RELAXATION

There are many textbooks which cover the basic concepts of nuclear magnetic resonance (NMR) and MRI physics; for rudimentary discussions see, for example, references [10-12], and for more advanced treatises the interested reader is referred to the texts by Haacke, *et al.* [13], Abragam [14], and Callaghan [15].

MR images portray the nuclear magnetic resonance (NMR) properties of certain nuclei; the most commonly studied nuclei in NMR include  $^1\text{H}$ ,  $^{13}\text{C}$ ,  $^{19}\text{F}$ ,  $^{23}\text{Na}$ , and  $^{31}\text{P}$ , where the superscript denotes the nucleon (mass) number, though this review is concerned exclusively with the  $^1\text{H}$  nucleus contained in water molecules. (The interested reader is referred to [16] for an introduction to non-proton NMR.) Each hydrogen nucleus possesses a magnetic moment, which means it behaves similar to a small bar magnet when placed in an external magnetic field. When tissues are immersed in a strong external magnetic field, these **magnetic nuclei tend to align with the field and thus a macroscopic magnetization is created within the sample**. It is this **net magnetization that is measured by all NMR techniques**. Measurements are made by the application of so-called **radiofrequency pulses**—short bursts of rapidly oscillating magnetic fields that vary at a specific “resonant” frequency which can change the direction of the macroscopic magnetization and thereby assess its magnitude. The size of the magnetization, and hence the **NMR signal measurable, is proportional to the water proton density**. However, the signal measured may also be affected by several other factors. In the absence of an external magnetic field, the nuclear magnets point in all directions with equal probability, so there is no net alignment. **Once the field is applied**, it takes a finite time for individual nuclei to re-orient and for the macroscopic magnetization to form within tissue. The **time for nuclei to align in this way is called the longitudinal or spin-lattice relaxation time  $T_1$** . This is also the time required for a magnetization that has been “disturbed” by a radiofrequency pulse to re-establish itself. Mathematically, this magnetization **parallel to the main magnetic field and usually taken to be in the  $z$ -direction** (denoted by  $M_z$ ) is modeled by the differential equation:

$$\frac{dM_z(t)}{dt} = \frac{1}{T_1} [M_o - M_z(t)], \quad (1)$$

with solution given by Eq. (2):

$$M_z(t) = M_o [1 - \exp(-t/T_1)]. \quad (2)$$

$T_1$  is several seconds in pure water but it is found to be much shorter for the water in solutions of macromolecules. In particular, the presence of proteins and other biopolymers affects the local viscosity and molecular dynamics of water such that the  $T_1$  of water in biological tissues are typically between 100-1000 milliseconds. MR images may be made **sensitive to variations in longitudinal relaxation times, and consequently the contrast in many MR images largely reflects variations in the concentrations and nature of macromolecules**—so-called  $T_1$ -weighted images.

The relaxation times of tissue water protons, which measures how long it takes nuclei to re-orient themselves in the presence of a field, is very sensitive to the local magnetic environment which they experience. In particular, the nuclear magnetic moment of a proton may interact with other magnetic fields at the molecular level, and as a result may change its orientation. The likelihood of this occurring depends on the nature and strength of local magnetic influences. Several metal ions, such as those of some transition elements such as iron, manganese and gadolinium, contained unpaired electrons in outer atomic orbits which generate very powerful magnetic fields on the atomic scale. These ions are said to be paramagnetic, and can exert a strong influence on other atoms and molecules in their immediate vicinity [9,17]. **Paramagnetic species such as gadolinium ions can thus induce water protons to alter their directions, so that the relaxation time of the net macroscopic magnetization is affected**. In practice, the relaxation rate (the reciprocal of the relaxation time) represents a probability of a nuclear magnet changing direction in any interval, and is **directly proportional** to the concentration of the paramagnetic species. Paramagnetic ions are used as MRI contrast agents because they change the relaxation times of water protons and thus **modulate the contrast in  $T_1$ -weighted images**. Quantitatively, in simple solutions, the increase in relaxation rate,  $1/T_1$ , produced by paramagnetic species is directly proportional to the molar concentration; the proportionality constant is termed the relaxivity and is usually measured in units of  $\text{sec}^{-1} \cdot \text{mM}^{-1}$  concentration. In practice this may vary with several factors including temperature, viscosity, proton exchange rate, and the presence of macromolecules [18, 19].

When a CA is introduced into the body, it decreases the relaxation times of the tissue water with which it comes into contact, which will depend on how the CA distributes within the tissues. The CA is typically administered as a bolus of fluid *via* a catheter injection into a peripheral vein (e.g., an antecubital in humans, tail or jugular in rodents). Once in the blood plasma it will distribute throughout the vasculature and may diffuse into tissues where it will alter the tissues native  $T_1$  value. If we consider a region of interest (ROI) and study the **temporal characteristics** of the signal intensity as the CA passes through the tissue, we can derive information

on tissue physiology and pathology. For example, such an approach allows for quantification of how much CA transiently “leaks” into the extravasculature space as well as the size of this space. Fig. (1) displays examples of signal intensity time courses taken from two ROIs within an invasive ductal carcinoma breast cancer. It is also possible to study blood flow and blood volumes with such techniques. Before discussing how such data can be analyzed, we first describe how such data can be acquired.

### 3. DCE-MRI DATA ACQUISITION

(To encourage uniform nomenclature in describing DCE-MRI we will employ only those symbols adopted by the community [20]).

In a typical DCE-MRI imaging session, a region of interest (ROI) is selected for study (e.g., a tumor locus), and MR images are collected before, during, and after a CA is injected into the antecubital vein of a patient or, in the case of an animal study, into a tail or jugular vein. Each image acquired corresponds to one time point, and each pixel in each image set then gives rise to its own time course (one signal intensity per time point) which can then be analyzed with a mathematical model. Values of various pharmacokinetic and intrinsic tissue properties may then be extracted by fitting (solid line in panel c) these time courses to produce parametric images. Model parameters, which describe the CA movement across the vascular endothelium, are expressed in typical physiological parameters: blood flow (perfusion), vessel wall permeability, vessel surface area, and extracellular extravascular volume fraction. To perform such an analysis, quantitative DCE-MRI data acquisitions require three measurements: 1) recording of a map of the native  $T_1$  values before contrast administration; 2) acquisitions of  $T_1$ -weighted images following CA

introduction at a reasonably high temporal resolution to be able to characterize the kinetics of the CA entry and exit into tissue; and 3) a method to estimate the time rate of change of the concentration of the CA in the blood plasma, the so-called arterial input function (AIF).

#### 3.1. Measuring Pre-contrast $T_1$ in Tissue

There are several choices for obtaining accurate measurements of  $T_1$ , but often these methods are time consuming and take too long for applications such as DCE-MRI. The most commonly used method of mapping  $T_1$  before administering the CA is to use a series of so-called spoiled gradient-recalled echo (SPGRE) images acquired with different degrees of  $T_1$ -weighting. For such an image the measured signal intensity is described by Eq. (3):

$$S = S_0 [\sin\alpha \cdot (1 - \exp(-TR/T_1))] \cdot \exp(-TE/T_2^*) / (1 - \exp(-TR/T_1) \cdot \cos\alpha) \quad (3)$$

where  $\alpha$ ,  $TR$ , and  $TE$  are all experimentally controlled;  $\alpha$  is the flip angle,  $S_0$  is a constant describing the scanner gain and proton density,  $TR$  is the repetition time,  $TE$  is the echo time, and  $T_2^*$  is the transverse relaxation time due to both molecular interactions and inhomogeneities in the external magnetic field. (Typically,  $TE \ll T_2^*$  so that the final exponential term can be taken as 1.) The idea is to collect SPGRE data at multiple flip angles (i.e., vary  $\alpha$  on successive acquisitions) and fit the data to Eq. (3) with  $S_0$  and  $T_1$  as floating parameters. This can be done on a voxel by voxel basis to construct a  $T_{10}$  (i.e., a map of  $T_1$  values before CA administration) map and an example of this approach is seen in Fig. (1b). Though this method is not without problems [21,22], it drastically decreases the total measurement time (for large volumes of interest) compared

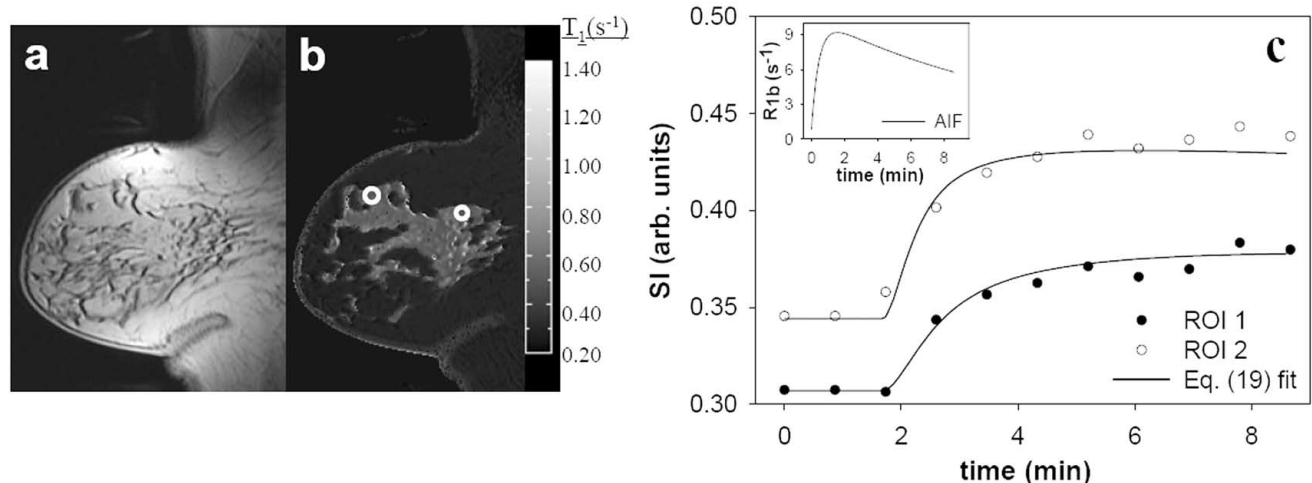


**Fig. (1).** A patient diagnosed with an invasive ductal carcinoma. Panel a is the pre-contrast injection  $T_1$ -weighted sagittal image and panel b is the  $T_1$  map; the lesion is easily delineated from the surrounding healthy-appearing tissue. Panel c depicts typical enhancement curves from two ROIs labeled on panel b. The leftmost white circle in panel b corresponds to the filled circles in panel c, while the rightmost white circle corresponds to the open circles in panel b. The fits of the data are depicted as the solid lines in panel c and the arterial input function (i.e., the time course of CA in the blood) used to perform those fits is shown in the inset. ROI 2 has a more rapid enhancement:  $K^{trans} = 0.063 \text{ min}^{-1}$  for ROI 1 and  $K^{trans} = 0.12 \text{ min}^{-1}$  for ROI 2. It is the ability to probe this intra-tumoral heterogeneity non-invasively and longitudinally that make these techniques potentially so powerful. Performing this type of analysis for every voxel allows the construction of the pharmacokinetic parameter maps of Fig. 6.



to many other methods, while still maintaining the high signal to noise (SNR) of those methods [13] and has been used by many investigators [see, e.g., 23-25]. Similar approaches have made use of gradient or spin echo images obtained at multiple repetition times [26,27]. Another method of obtaining the pre-contrast  $T_1$  map involves obtaining a **proton density-weighted image and a  $T_1$  weighted image and then considering their ratio** [28]. Rapid, quantitative mapping of tissue  $T_1$  is still a field of active investigation and the interested reader is referred to references [29-31].

### 3.2. Dynamic Data Acquisition

After acquiring the  $T_1$  map, heavily  $T_1$ -weighted images must be acquired serially before and after the administration of the CA. To achieve heavily  $T_1$ -weighted images at rapid temporal resolution requires making compromises in the image quality or the range of tissue (number of slices) that can be interrogated. Serial images must be acquired with **sufficient temporal resolution to characterize the CA enhancement characteristics of the tumor under investigation**, but at the same time must be acquired with high enough spatial resolution so that the **inherent heterogeneity of the lesion can be adequately probed**. In MRI (or any imaging experiment), there is a trade-off between temporal resolution, spatial resolution, and signal to noise; when designing a DCE-MRI experiment, these needs must be carefully balanced. To satisfy all of these often conflicting demands, DCE-MRI experiments almost exclusively employ multi-slice or 3D sequences that can be acquired rapidly and which allow for *relatively* high-temporal, signal-to-noise, and spatial resolution.

Temporal resolution in these experiments can be as rapid as 1 second, though most studies employ temporal resolution in the 10-30 second range. **Coarser temporal resolution allows for obtaining a larger acquisition matrix over a fixed field of view and this allows for higher spatial resolution** with higher in-plane and through plane resolution. Some investigators emphasize high spatial resolution [32] over high temporal resolution [33]. In such cases the spatial resolution can (currently) approach approximately 0.50 mm (in plane resolution) compared to approximately 1.7 mm obtained in studies where temporal resolution is emphasized. High spatial resolution is typically selected if a “semi-quantitative” analysis is planned (see below) and probing tumor heterogeneity at the finest possible level is viewed as very important, while the high temporal resolution approach is selected if a full quantitative analysis is planned and the CA kinetics need to be finely sampled to allow for accurate model-fitting. In designing a DCE-MRI data acquisition protocol one needs to consider the goals of the study and carefully select the appropriate study parameters balancing the needs of the study with resolution issues.

### 3.3. Measuring the Arterial Input Function

The most technically demanding portion of the data acquisition process in DCE-MRI is acquiring an estimate of the concentration of the contrast agent in the blood plasma as a function of time,  $C_p(t)$ , the AIF. As detailed in the Data Analysis section below, knowledge of the AIF is required to perform nearly all of the currently available methods of

quantitative DCE-MRI data analysis—though recent developments have the potential to remove this necessity and are discussed below. To date, three main approaches have been developed to estimate the AIF. One approach involves introducing an arterial catheter into the subject and sampling blood during the imaging process for later analysis [34,35]. An advantage of this approach is that the  $C_p$  in each sample can be determined through standard chemical analytic methods thereby allowing for very accurate characterization of  $C_p$  as a function of time. However, the disadvantages include its invasive nature, poor temporal resolution, and relative ambiguity concerning the actual time at which the sample was drawn. In laboratory mice, which are used in many DCE-MRI experiments, the total blood volume is very small (~2 mL) so that **very few samples (2–5; assuming a volume of 50–100  $\mu$ L per sample) can be taken** in total and fewer still can be used to characterize the uptake portion of the  $C_p$  curve.

A second method assumes that the AIF is similar for all subjects. The **AIF is first measured** via blood samples in a small cohort of subjects, and the **resulting average AIF** is then assumed to be valid for subsequent studies [36,37]. A major advantage of this approach is its simplicity in both data acquisition and data analysis; no AIF measurement is required for the experimental subjects, and the subsequent curve-fitting uses a common AIF on all data sets. The disadvantages include the influences of both inter- and intra-subject variations in AIF which can introduce large errors in both AIF characterization and the subsequent pharmacokinetic analysis [35]. Also, by measuring the AIF in one cohort of subjects and applying it to another, changes in the AIF which may be introduced by the pathology under investigation are ignored, reducing the validity of the assumption in important practical situations.

A third method obtains the AIF from the DCE-MRI data sets themselves [38-42]. Methods have been developed that simultaneously measure signal intensity changes (due to CA passage) in both the blood and tissue. A calibration is then employed to **convert the blood signal intensity to the intravascular concentration of CA**. Such a method has the potential advantage of measuring the AIF accurately on an individual basis and, since it does not require any further measurements, being completely non-invasive. However, it requires the presence of a large vessel within the field of view [43]. Additionally, the images must be acquired such that the **lumen signal faithfully reflects variations only in the CA concentration and not other factors (e.g., partial volume or flow effects)**. This restricts the regions that can be characterized, the imaging slice orientation, and (as the data are often acquired using ultra-fast imaging techniques) greatly reduces the ability to acquire images with both high spatial resolution over a large section of tissue and signal-to-noise ratio. The former is potentially an especially important drawback as a major use of DCE-MRI is to assess heterogeneous tissues such as tumors which demand high spatial resolution.

Recently, some investigators have begun to develop and apply **“reference region models”** [44-46]. These models, which have their root in the positron emission tomography literature [47], rely on calibrating signal intensity time

courses in the tumor to that in a well-characterized reference region (typically muscle), thereby eliminating the requirement for AIF measurement. These models will be discussed below.

In summary, to obtain DCE-MRI data, three main components of data are required: 1) a  $T_1$  map before the administration of the CA; 2)  $T_1$ -weighted images obtained with a temporal resolution of between 5 and 60 seconds; 3) a method for estimating the arterial input function. With such data in hand, we now discuss the currently available methods of data analysis.

#### 4. DCE-MRI DATA ANALYSIS

Though the division is somewhat arbitrary, we will define any technique that requires measurement of  $T_{10}$  and characterization of the AIF (either implicitly or explicitly) as “quantitative”, and those techniques which do not require those measurements as “semi-quantitative.” All methods are quantitative in the sense that a number is returned at the end of the analysis but, in principle, the methods we have chosen to define as quantitative involve more rigorous theory and modeling and thus should more accurately reflect physiology than the semi-quantitative methods. However, the additional rigor comes at a price; in addition to being technically more demanding (in both data acquisition and analysis), such methods may not be as reproducible, repeatable, or robust to noise as some of the semi-quantitative methods. As in choosing a data acquisition protocol, the goals of the experiment must be considered when choosing a data analysis method. If only relative changes are required, then a semi-quantitative approach may suffice.

##### 4.1. Quantitative Models

Quantitative analysis of DCE-MRI data is intimately connected with the study of the pharmacokinetics of CA's, particularly their distribution within and elimination from the body [48,49]. When a CA is introduced into a patient or animal, it may be subject to a series of processes that include distribution into the bloodstream and tissue spaces, interaction with any targeted receptor sites/ligands, metabolism and then elimination by excretion (e.g., small molecule gadolinium-based CAs are removed by the kidneys with a half life of approximately 90 minutes in humans, and 27 minutes in mice). In order to characterize these complex processes, a model that describes the underlying biology must be developed to allow for mathematical analysis. Fitting the DCE-MRI time course with such models can be used to extract knowledge of the underlying physiology and/or pathology. Typical physiological parameters describing the CA movement across the vascular endothelium include: blood flow (i.e., perfusion), vessel wall permeability, vessel surface area, intravascular and extravascular volume fractions.

Pharmacokinetic analysis of an exogenous CA experiment is based on several assumptions. The principal assumption is that the human body may be represented by one or more “compartments”, into and out of which the CA dynamically flows. A compartment may be defined as a bounded space that the CA can occupy and whose volume remains constant on the time scale of the DCE-MRI experiment. A second common underlying assumption is that each

compartment is assumed to be “well-mixed” in the sense that CA entering the compartment is immediately distributed uniformly throughout the entire compartment.

The simplest pharmacokinetic model depicts the body as a single compartment with fixed volume and such an approach is depicted in Fig. (2a). The drug arrives at the compartment volume,  $V$ , with a specific rate constant  $k_a$ , and is eliminated with a rate constant  $k_e$ . If the drug under consideration is assumed to reach an equilibrium concentration throughout the body, then such an approach is fruitful. However, CAs are typically distributed at different rates in different tissues and these kinetics are more realistically described by a two-compartment model.

A two compartment model considers the intravascular extracellular volume fraction (blood plasma) to be the central compartment ( $V_1$ ), and the extravascular-extracellular volume fraction ( $V_2$ ) to be the peripheral compartment. In this model, the CA is introduced into the vasculature and diffuses into the extravascular-extracellular space in a reversible process characterized by a distribution rate constant ( $k_{12}$ ) and a redistribution rate constant ( $k_{21}$ ) as presented in Fig. (2b). The CA is eliminated in an irreversible process described by the rate constant  $k_e$ . The parameters of interest are typically taken to be  $K^{trans}$  (the distribution rate constant),  $v_e$  (the extravascular-extracellular volume fraction), and  $k_{ep}$  (the redistribution rate constant). These parameters have been shown to reveal diagnostic and prognostic information.

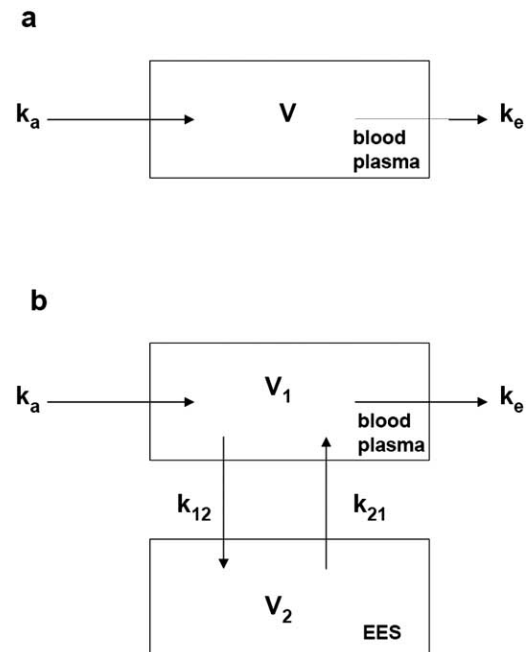


**Fig. (2).** The simplest pharmacokinetic model is depicted in panel a. A drug enters the compartment,  $V$ , with a specific rate constant  $k_a$ , and is eliminated with a rate constant  $k_e$ . A more realistic approach is described by the two-compartment model depicted in panel b which considers the extracellular intravascular space (blood plasma) to be the central compartment ( $V_1$ ), and the extravascular-extracellular space (EES) to be the peripheral compartment ( $V_2$ ). In this model, the CA is introduced into the vasculature and transported into the EES in a reversible process characterized by a distribution rate constant ( $k_{12}$ ) and a redistribution rate constant ( $k_{21}$ ).

The two compartment model most frequently employed in the modeling of DCE-MRI data sets is based on the formalism pioneered by Seymour Kety in 1951 [38]. The model is characterized by the CA concentrations in tissue,  $C_t$ , arterial blood,  $C_b$ , and two first order kinetic rate constants, (say)  $k_{12}$  and  $k_{21}$ . We assume that within each compartment (blood and tissue) the CA is homogeneously distributed. Let the unidirectional CA flux, at time  $t$ , from the blood to tissue be  $k_{12} \cdot C_b(t)$ , and the flux from tissue to blood be  $k_{21} \cdot C_t(t)$ . Thus, the net CA flux into tissue is given by Eq. (4):

$$\frac{d}{dt} C_t(t) = k_{12} \cdot C_b(t) - k_{21} \cdot C_t(t) \quad (4)$$

The physiological interpretation of  $k_{12}$  is the product of blood flow,  $F$ , and extraction fraction,  $E$ ; i.e.,  $k_{12} = E \cdot F$ . The rate constant  $k_{21}$  will be defined below. By defining an appropriate integrating factor, Eq. (4) becomes an exact equation which can then be integrated directly (see, e.g., [50]) to obtain Eq. (5):

$$C_t(T) = k_{12} \cdot \int_0^T C_b(t) \cdot \exp(-k_{21} \cdot (T-t)) dt \quad (5)$$

Now consider an experiment in which  $C_b(t)$  is maintained at a constant concentration for a specified period of time. Over time,  $C_t$  will increase to a maximum at which point the net tracer flux is zero and the system is in “equilibrium.” At this equilibrium point,  $C_b(t_{\text{equilibrium}})$  and  $C_t(t_{\text{equilibrium}})$  are constant (but not, in general, equal) and their ratio,  $C_t/C_b$  is termed the “partition coefficient”,  $\lambda$ . Thus, at equilibrium, we must have  $(d/dt)C_t = 0$ , from which Eq. (4) implies Eqs. (6) – (8):

$$k_{12} \cdot C_b = k_{21} \cdot C_t \quad (6)$$

$$\Leftrightarrow k_{12}/k_{21} = C_t/C_b \equiv \lambda \quad (7)$$

$$\Leftrightarrow k_{21} = k_{12}/\lambda = E \cdot F/\lambda. \quad (8)$$

In the literature [51,52],  $\lambda$  is often expressed (for these two compartments) as in Eq. (9):

$$\lambda = v_e/(1-h), \quad (9)$$

where  $h$  is the hematocrit. With these assignments, we can write Eq. (10):

$$k_{21} = E \cdot F \cdot (1-h)/v_e. \quad (10)$$

The MRI pharmacokinetic community [20] has defined the quantity  $E \cdot F \cdot (1-h) \equiv K^{trans}$ . Thus, use of this definition and substitution of Eq. (10) into (5) yields

$$C_t(T) = K^{trans} \cdot \int_0^T C_p(t) \cdot \exp(-K^{trans}/v_e \cdot (T-t)) dt, \quad (11)$$

where we have also made use of the relation  $C_p(t) = (1-h) \cdot C_b(t)$  where the subscript “ $C_p$ ” indicates concentration of the agent in the blood plasma. The physiological interpretation of  $K^{trans}$  is dependent upon the rate limiting step in the delivery of the contrast agent to the voxel of interest; if blood vessel permeability is much greater than

perfusion, then the system is said to be perfusion limited, whereas if perfusion is much greater than vessel permeability then the system is said to be permeability limited [20].

Several investigators [53,54] have pointed out that Eq. (11) simplifies the analysis by not explicitly including a (blood) plasma compartment,  $v_p$ , that may be present in a given voxel of tissue and therefore amend this equation to read:

$$C_t(T) = K^{trans} \cdot \int_0^T C_p(t) \cdot \exp(-K^{trans}/v_e \cdot (T-t)) dt + v_p \cdot C_p(t). \quad (12)$$

Eqs. (11) and (12) are the basis of the majority of quantitative DCE-MRI experiments currently being reported in the literature, but frequently not in the form presented here. The general approach is to measure  $C_p$  and  $C_t$  time courses and perform a nonlinear least squares fit of Eq. (11) or (12) to such data. By varying the parameters in those equations, one can obtain estimates on  $K^{trans}$  and  $v_e$ . We note here that another group of models described as distributed parameter models are used to a lesser extent and report on similar parameters. The interested reader is referred to, for example, references [55-60].

Since CA detection is indirect, via CA enhancement of water proton NMR relaxation, the relation between concentration of CA and the measured  $^1\text{H}_2\text{O}$  NMR signal must be known. The apparent longitudinal relaxation rate constant,  $R_1$  ( $\equiv 1/T_1$ ), is in principle proportional to  $C_t(t)$  so that it is usual to assume that [61]:

$$R_1(t) = r_1 \cdot C_t(t) + R_{10}, \quad (13)$$

Where,  $r_1$  is the CA relaxivity and  $R_{10}$  is the pre-CA longitudinal relaxation rate constant. Substituting Eq. (11) or (12) into Eq. (13) yields equations which can be fit to DCE-MRI to extract the parameters present in each model ( $K^{trans}$  and  $v_e$  for Eq. (11);  $K^{trans}$ ,  $v_e$ , and  $v_p$  for Eq. (12)) if  $R_1$  time courses can be measured. Several variations on these equations have been developed and presented in the literature.

The need for high temporal resolution in DCE-MRI studies does not allow for direct measurement of an  $R_1$  time course, thus  $R_1(t)$  is typically estimated from the signal intensity time course and the  $T_{10}$  map described above. That is, if  $T_{10}$  is known, then taking the ratio of  $S_n$  to  $S_1$  (the  $n^{\text{th}}$  signal intensity to the first) yields an expression which can analytically be solved for  $T_{1n}$ , the  $T_1$  value at the  $n^{\text{th}}$  time point. The  $T_1$  ( $\equiv 1/R_1$ ) time courses can then be converted to CA time courses via relations similar to Eq. (13), and then analyzed with equations similar to (11) and (12).

Eq. (13) is, of course, a simplification and the application of such models to biological tissue presupposes that the interstitium behaves as a well-mixed, homogeneous solution with respect to the CA; or, equivalently, that the system remains in what is typically called the fast exchange limit (FXL) with respect to the water exchange between two regions. We now explore the implications of this assumption.

Tissue parenchyma is not a single homogeneous solution, but is highly compartmentalized on the scale of a MR image



voxel [62]. In most tissues, most water is intracellular [62], and thus cannot directly access the CA molecule. The use of a linear Eq. (13) for the entire  $^1\text{H}_2\text{O}$  signal from a voxel requires that water exchange between compartments be sufficiently fast compared with the relaxation rate constants in each compartment so that the water exchange system is in the FXL. (This is equivalent to treating the CA as if it were distributed uniformly throughout the voxel.) However, it has been shown that, though fast, water exchange is insufficiently frequent for this assumption to be true at all  $C_t(t)$  values following a CA injection [61]. In this case, the longitudinal  $^1\text{H}_2\text{O}$  relaxation can, in principle, exhibit a bi-exponential experimental decay. McConnell [63], Woessner [64], and Lee [65] developed equations that explicitly incorporate the effects of slower water exchange. In this case, the longitudinal  $^1\text{H}_2\text{O}$  relaxation can be characterized as exhibiting a bi-exponential decay and Eqs. (3) and (13) must be altered to account for this, thus:

$$S/S_0 = a_L[\sin\alpha(1 - E_{1L})/(1 - E_{1L}\cos\alpha)] + a_S[\sin\alpha(1 - E_{1S})/(1 - E_{1S}\cos\alpha)], \quad (14)$$

where  $E_{1L} \equiv \exp(-TR/T_{1L})$ , and  $E_{1S} \equiv \exp(-TR/T_{1S})$ ,  $S$  is the measured, instantaneous signal intensity,  $S_0$  is the signal intensity representing fully-relaxed magnetization,  $a_L$  and  $R_{1L}$  are the fraction and  $1/T_1$ , respectively, for the component with the longer  $T_1$  (i.e.,  $T_{1L} \equiv 1/R_{1L}$ );  $a_S$  and  $R_{1S}$  are defined similarly for the component with the shorter  $T_1$ .

Modeling this system requires accounting for the exchange of water molecules from compartment  $A$  to compartment  $B$  and we write equations (15) and (16) which are analogous to Eq. (1):

$$\frac{dM_{zA}(t)}{dt} = \frac{1}{T_1}[M_0 - M_{zA}(t)] \quad (15)$$

$$\frac{dM_{zB}(t)}{dt} = \frac{1}{T_1}[M_0 - M_{zB}(t)], \quad (16)$$

where  $M_{zA}$  denotes the  $z$  component of nuclear magnetization in compartment  $A$ ,  $T_{1A}$  is its longitudinal relaxation time, and  $M_{0A}$  is its equilibrium magnetization. Analogous definitions apply to the “ $B$ ” environment. In 1958, McConnell [63] showed how Eqs. (15) and (16) could be directly generalized to include the effects of exchange of nuclear spins between the two environments:

$$\frac{dM_{zA}(t)}{dt} = [M_{0A} - M_{zA}(t)]/T_{1A} - \frac{M_{zA}}{\tau_A} + \frac{M_{zB}}{\tau_B} \quad (17)$$

$$\frac{dM_{zB}(t)}{dt} = [M_{0B} - M_{zB}(t)]/T_{1B} - \frac{M_{zB}}{\tau_B} + \frac{M_{zA}}{\tau_A}, \quad (18)$$

where  $\tau_A$  denotes the average lifetime of a spin in compartment  $A$ , and  $\tau_B$  denotes the average lifetime in the

compartment  $B$ . In Eq. (17), the  $-\frac{M_{zA}}{\tau_A}$  term measures the

rate at which  $M_{zA}$  decreases due to transfer out of

compartment  $A$  and, similarly, the  $+\frac{M_{zB}}{\tau_B}$  term measures

the rate at which  $M_{zA}$  increases due to transfer into compartment  $A$ . Similar comments apply to Eq. (18).

Eqs. (17) and (18) constitute a pair of linear homogeneous differential equations for which a solution is readily available. For the system above, the solutions are given by:

$$1/T_{1S,1L} = 1/2(1/T_{1A} + 1/\tau_A + 1/T_{1B} + 1/\tau_B) \pm [1/4(1/T_{1A} + 1/\tau_A + 1/T_{1B} + 1/\tau_B)^2 - ((1/T_{1A} + 1/\tau_A)(1/T_{1B} - 1/\tau_B) - 1/\tau_A\tau_B)]^{1/2}. \quad (19)$$

This derivation was first accomplished by Woessner in 1961 [64]. Eq. (19) has found two primary applications in the DCE-MRI literature to date: one in which compartments  $A$  and  $B$  are the vascular and extravascular extracellular spaces, respectively [66-69]; and one in which compartments  $A$  and  $B$  are the extravascular extracellular space and the extravascular intracellular space, respectively [70-71]. Combining Eq. (19) with Eq. (11) can return estimates on  $K^{trans}$ ,  $v_e$ , and the intravascular lifetime of a water molecule, while the second returns estimates on  $K^{trans}$ ,  $v_e$ , and the extravascular intracellular lifetime of a water molecule. The expressions for the  $a_S$  and  $a_L$  in Eq. (14) are cumbersome and the interested reader is referred to the papers cited above for their form. This formalism has only recently been applied in assessing longitudinal changes in tumor characteristics [72] and as a retrospective analysis of diagnosing malignant versus benign breast tumors [73]. Some applications of these more rigorous models to analyze DCE-MRI cancer data are beginning to appear [70,71,74]. Additionally, a more comprehensive approach has been offered which accounts for water exchange between all three sites [75].

As mentioned above in section 2.3, some models do not require measurement of the arterial input function. These models are based on calibrating the tissue changes to that found in a more stable “reference tissue”. Kovar, *et al* [44] were the first to introduce such an approach and employed the differential form of the Kety law (i.e., Eq. (4)) by assuming particular (literature supported)  $K^{trans}$  and  $v_e$  values for a muscle ROI and using the measured  $C_t(t)$  curve for the same ROI to calculate a  $C_p(t)$  time course. This AIF could then be used for an Eq. (11) analysis of the tumor to extract  $K^{trans}$  and  $v_e$  for the tumor on either a ROI or voxel-by-voxel basis. This model was recently augmented [45] by completely eliminating the need to explicitly characterize the AIF; this is done by considering two copies of Eq. (4), one for the reference region (RR) and one for the tissue of interest (TOI):

$$\frac{d}{dt} C_{RR}(t) = K^{trans,RR} \cdot C_p(t) - (K^{trans,RR}/v_{e,RR}) \cdot C_{RR}(t) \quad (20)$$

$$\frac{d}{dt} C_{TOI}(t) = K^{trans,TOI} \cdot C_p(t) - (K^{trans,TOI}/v_{e,TOI}) \cdot C_{TOI}(t) \quad (21)$$

where  $C_{RR}$  and  $C_{TOI}$  are the tissue concentrations (expressed in mM) of CA in the RR and the TOI, respectively;  $K^{trans,RR}$  and  $K^{trans,TOI}$  are the CA extravasation rate constants for the RR and TOI, respectively; and  $v_{e,RR}$  and  $v_{e,TOI}$  are the extravascular extracellular volume fractions for the RR and TOI, respectively. Solving Eq. (20) for  $C_p(t)$  and substituting the result into Eq. (21) yields a differential equation that is independent of  $C_p(t)$ . Again, by defining an appropriate integrating factor the differential equation can be made exact and integrated directly to yield the operational equation:

$$C_{TOI}(T) = R \cdot C_{RR}(T) + R \cdot [(K^{trans,RR}/v_{e,RR}) - K^{trans,TOI}/v_{e,TOI}] \cdot \int_0^T C_{RR}(t) \cdot \exp((-K^{trans,TOI}/v_{e,TOI}) \cdot (T-t)) dt, \quad (22)$$

which can then be fit to measured TOI and RR kinetic data to extract  $K^{trans}$  and  $v_e$  of the TOI. This is done by fixing either or both of  $K^{trans,RR}$  and  $v_{e,RR}$  and floating the remaining parameters. (Eq. (13) or (19) can be used to convert from measured signal intensity to concentration of CA.) Since AIF characterization is not required, an advantage of this approach is that the acquisition process is much simpler and time can be spent on obtaining high spatial resolution and high signal-to-noise ratio data. This is possible because the enhancement kinetics in tissue are much slower than that of the blood plasma and slower temporal resolution are required [33]. Details in the derivation and application of Eq. (22) are provided in reference [45] and a similar approach employing multiple reference sites is presented in [46].

#### 4.2. Semi-Quantitative Models

Since the quantitative methods described above can be quite complex to implement, a set of more easily implemented analysis routines have been developed. Common parameters returned from a “semi-quantitative” analysis include the initial area under the curve (iAUC), the time to peak (TTP), and the slope of the washout curve [76]. These parameters are easily accessible with simple computer routines and many investigators have used them successfully to monitor cancer growth and treatment response (see below for examples from the literature). Walker-Samuel, *et al*, have explored the relationship between the quantitative parameters and the semi-quantitative parameters and found that the iAUC can display correlations with  $K^{trans}$ ,  $v_e$ , and  $v_p$  [77]. Thus, the simple, semi-quantitative parameters do report on physiology but in a mixed fashion; in fact, the authors conclude that the initial area under the curve “has an intractable relationship with all three” parameters [77]. Thus, the iAUC is not uniquely valued; that is, different combinations of  $K^{trans}$ ,  $v_e$ , and  $v_p$  can lead to the same value of iAUC so that any observed change in iAUC could result from a variety of phenomena [77].

However, these methods have the obvious advantage of being very straightforward to implement and can be

performed in near real-time. Their obvious limitations include the fact that the semi-quantitative parameters do not necessarily have clear physical correlates since they are “mixed” measures; e.g., while the iAUC does indeed reflect tissue blood flow and vascular permeability, it is also an indirect measure of the fractional interstitial space. Additionally, the degree to which each of these physiological parameters contributes to the iAUC is at least partially determined by what time point is (arbitrarily) taken as the end of the initial portion of the enhancement curve; in this light, they are not pure measures of “physiology”. It should also be noted that since these methods rely on signal intensity measurements (and not a physical measurement like  $T_1$ ), it is inherently difficult to compare quantitatively scans performed at separate times. For this reason, semi-quantitative methods are also difficult to compare between institutions.

There have also been successful applications of simply applying “curve-ology” to DCE-MRI time courses. That is, merely considering the shape of the uptake and washout of contrast agent [78,79]. This approach has been particularly successful in breast imaging [80].

#### 4.3. Statistical Models

Recently there have been developments of the application of statistical models to analyze CA kinetics. These efforts, thus far, attempt to circumvent the difficulties in both data acquisition and analysis in the methods described above; in particular, it is a well known difficulty that the quantitative models described above will not always converge when fitting procedures are performed. Another confounding issue in the application of the above techniques is the amount of variation currently present in the interpretation of DCE-MRI data for assessing malignancy or response to treatment [81]. Statistical approaches offer the potential to eliminate this subjectivity. At the expense of higher computational cost, statistical models have the potential to offer improved accuracy and offer an alternative to the problems of convergence [82] and user interpretation. Statistical methods have been developed which can produce accurate measurements on tumor size and return estimates on the same quantitative parameters enumerated above (i.e.,  $K^{trans}$ ,  $v_e$ , and  $v_p$ ). These models do so not by employing a nonlinear regression (least-squares) best fit of a model equation to observed data but by, for example, employing Bayesian statistics to estimate parameter values for each voxel [82]. Another approach employs clustering algorithms to separate enhancement kinetics into various classes with similar characteristics. Enhancement patterns (e.g., uptake rate, time to peak, washout slope, etc.) are then extracted and these features are used to distinguish between benign and malignant [83]. These approaches yield results comparable to the more accepted measures described above without presupposing an explicit physiological model [84]. This latter characteristic is particularly attractive as all of the models described above require some set of assumptions (all of which may not be justified and all of which represent gross simplifications of the underlying physiology) which may or may not be accurate. The recent efforts on statistical approaches are very promising and it is anticipated that these



models will find general use in both diagnostics and assessing longitudinal DCE-MRI data.

### 5. EXAMPLE APPLICATIONS

There are numerous papers in the literature employing the techniques described above. Here we present few illustrative examples of some of these techniques, describe a series of (representative) pre-clinical and clinical studies, and refer the interested reader to several recent manuscripts in which these techniques were employed in oncology studies.

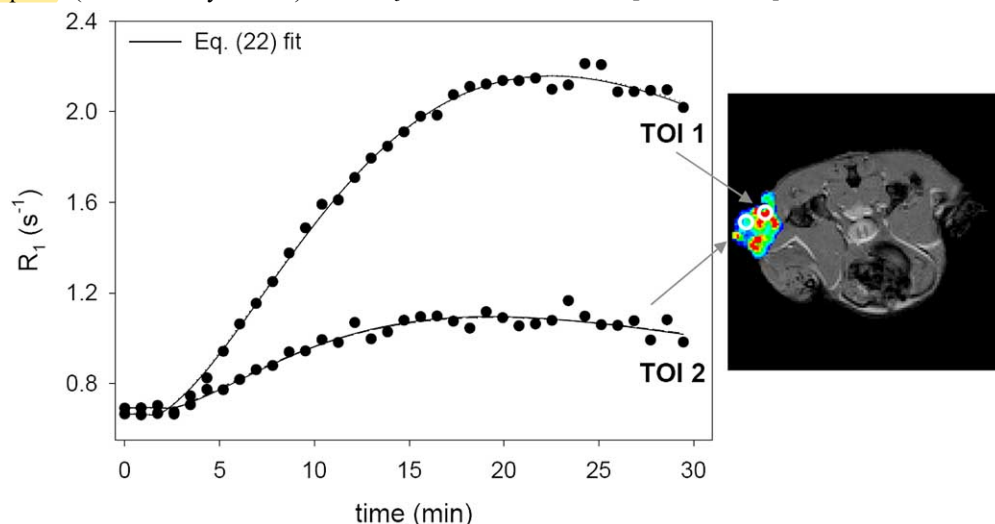
Fig. (3) shows the results of fitting two nine voxel ROIs (filled circles) taken from time courses obtained 16 days after the implantation of a 4T1 mammary carcinoma in the hind limb of a mouse. The solid lines represent the fit of the data to Eq. (22). Assuming  $v_{e,RR} = 0.08$  [66], the top curve yields values of  $K^{trans,RR} = 0.045 \pm 0.005$ ,  $K^{trans,TOI} = 0.077 \text{ min}^{-1} \pm 0.006$ , and a  $v_e$  value of  $0.70 \pm 0.024$ . Analysis of the bottom curve with Eq. (22) returned values of  $0.041 \pm 0.006$  and  $0.17 \pm 0.004$ . Regarding a more semi-quantitative description of these curves, note that the iAUC is much greater for the top curve and that it reaches its peak at approximately 22 minutes, whereas the lower curve exhibits a lower iAUC and a peak enhancement at approximately 18 minutes. (A comparison of the Eq. (11) and Eq. (22) is presented in reference [42]).

Fig. (4) depicts the results of such an analysis applied longitudinally to an entire tumor region. The figure shows three rows, each one corresponding to an imaging day and presenting the results of the parametric  $v_e$  (Fig. 4a) and  $K^{trans}$  (Fig. 4b) tumor mappings of a central slice as well as the corresponding 3-D volume representations. (Note the color scale on the far right and the distance scale in the lower right hand corner of each  $K^{trans}$  volume rendering.) By day 20 after tumor inoculation there is a  $15.5 \pm 1.34 \text{ mm}^3$  tumor that is well-vascularized with high perfusion and/or permeability as evidenced by the large number of red pixels indicating  $K^{trans} > 0.30 \text{ min}^{-1}$  (Fig. 4b and d) throughout the entire tumor. At this time point the tumor also has an increased extravascular-extracellular space (over healthy tissue) with  $v_e$  values

clustered between 0.2 and 0.4 (Fig. 4a and c). By day 24, the tumor has grown to  $67.4 \pm 3.47 \text{ mm}^3$  and only the periphery of the tumor is well vascularized as seen by both the red pixels in the  $K^{trans}$  map (Fig. 4f) and the volume rendering (Fig. 4h). Additionally, the  $v_e$  (Fig. 4e) map displays reduced values (0.1 to 0.3) as the extravascular extracellular volume fraction begins to shrink and is (probably) replaced by necrotic regions; a similar pattern is seen throughout the tumor (Fig. 4g). By day 33 the tumor has reached  $536.0 \pm 28.4 \text{ mm}^3$  and the central region has become necrotic as evidenced by many voxels that do not display significant enhancement. On the  $K^{trans}$  map (Fig. 4j) and volume rendering, the extreme periphery of the tumor contains many red pixels and therefore is still well vascularized. There are elevated values in the  $v_e$  parametric map (Fig. 4i) and volume rendering, but these voxels are located almost entirely within the tumor rim. Moving towards the tumor core,  $v_e$  clusters around 0.05 – 0.10 indicating a large intracellular volume fraction in those voxels that do support modeling. These parametric mappings and volume representations are instructive for identifying “hot spots” of tumor activity, probing tumor heterogeneity, and assessing longitudinal changes.

Such an analysis is appropriate for longitudinal assessment of tumor treatment response and an example is presented in Figure (5). The figure depicts  $K^{trans}$  maps of the central axial slice on days 8, 11, and 16 after  $10^6$  4T1 carcinoma cells were injected in the hind limb of a mouse; the top row is the control animal while the bottom row received  $4 \times 10^9$  plaque forming units of both AdAng2 (an anti-normalization drug) and AdExFlk (an anti-angiogenesis drug) on day 9. By day 16 the tumor in the control mouse is significantly more highly perfused and permeable vessels as estimate by  $K^{trans}$  than the treated animal does. This type of analysis is frequently employed in the literature and several examples are discussed below.

A clinical example of DCE-MRI assessment of treatment response is presented in Fig. (6). Since data can be obtained for multiple slices acquired to cover the whole breast, 3D



**Fig. (3).** The results of fitting two arbitrary nine voxel TOI curves (solid circles) with both the Eq. (22) (solid curve) model. The different curve shapes yield different  $K^{trans}$  and  $v_e$  values as discussed in the text.

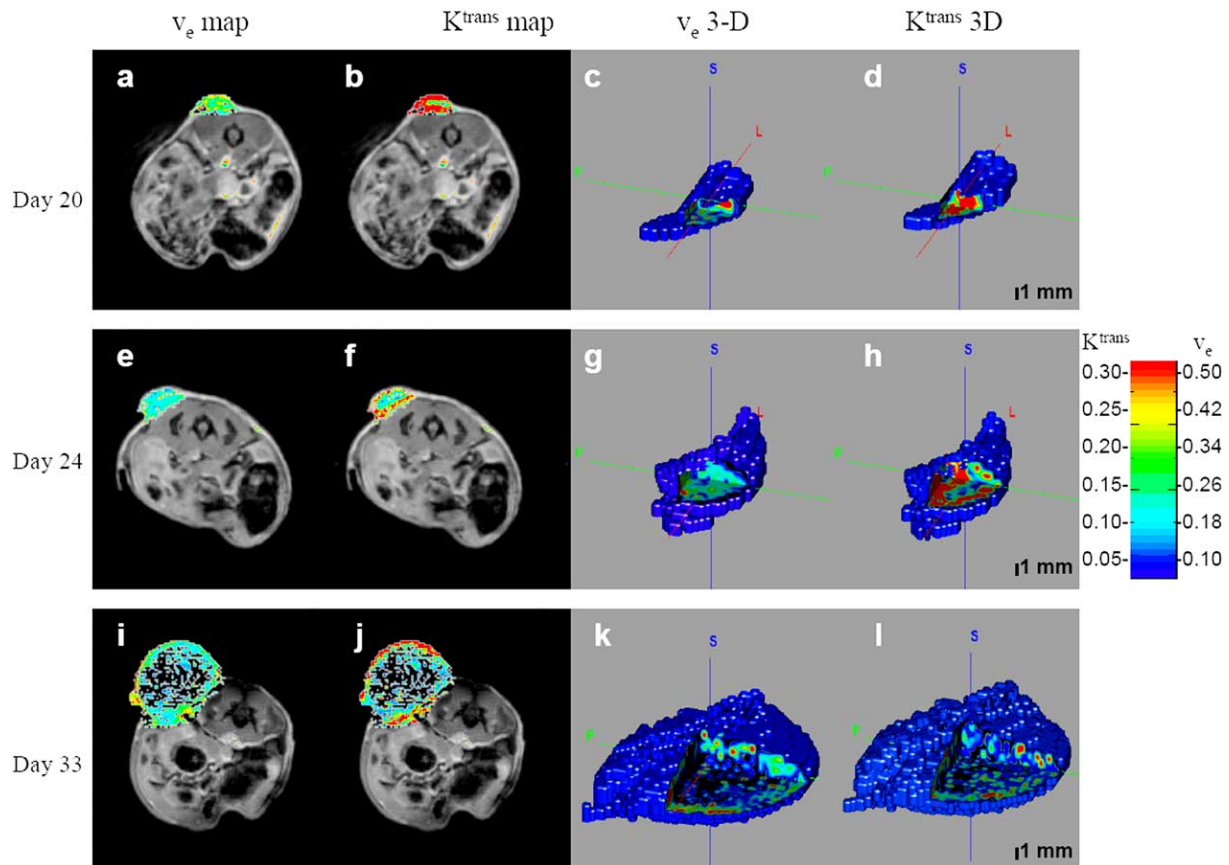


**Fig. (4).** The results of applying a DCE-MRI protocol to the entire tumor region as a function of time. Each row corresponds to an imaging day and presents the results of the parametric  $v_e$  (a, e, i) and  $K^{trans}$  (b, f, j) tumor mappings of a central slice as well as the corresponding 3-D volume representations ( $v_e$ : c, g, k;  $K^{trans}$ : d, h, l). Note the color scale on the far right and the distance scale in the lower right hand corner of each  $K^{trans}$  volume rendering. See text for discussion of parameter changes as a function of time.

volume representations can be constructed. The first column displays the 3D renderings, while the second column displays the central slice of the lesion as estimated by the  $K^{trans}$  parametric map. The top row presents the pre-treatment  $K^{trans}$  volume renderings for the same patient depicted in Fig. 1 and the bottom row is the post-treatment (Taxotere for four cycles)  $K^{trans}$  volume rendering. This analysis employed the AIF depicted in the inset of Fig. 1c and combined with Eqs. (11) and (19). Cut-aways are displayed to give an indication of where the tumor is spatially located within the breast. Both volumes are rendered at 50% of the maximum value measured on the pre-treatment study. Of particular interest is the reduction in the number of voxels displaying elevated  $K^{trans}$  values post-treatment seen in both presentations. For details of this study, the interested reader is referred to [85].

We now present brief summaries of four representative pre-clinical studies and four representative clinical studies which employed DCE-MRI as a quantitative biomarker.

### 5.1. Pre-Clinical Studies

de Lussanet, *et al*, recently monitored the anti-angiogenic effects of the novel drug anginex and the established angiogenesis inhibitor TNP-470 [86] with DCE-MRI. Anginex has been shown to prevent both the migration and adhesion of endothelial cells *in vitro* [87], while *in vivo* work has shown that anginex inhibits angiogenesis without side

effects [88]. TNP-470 has exhibited anti-angiogenic characteristics as manifested by its ability to inhibit angiogenesis both *in vitro* and *in vivo* [89]. The authors thus hypothesized the two anti-angiogenic drugs would lead to decreased tumor microvessel density as measured by histology and that this pattern would be seen in  $K^{trans}$  (though the authors refer to the parameter as  $K^{PS}$ , a name that has been selected for replacement by  $K^{trans}$  by the DCE-MRI community [20]) as measured by DCE-MRI. Mice were inoculated with  $2 \times 10^5$  B16F10 cells to induce melanomas and then divided into three groups: group one ( $n=5$ ) was treated with Anginex at the dose of 6mg/kg body weight per day beginning on day zero; group two ( $n=3$ ) was treated with TNP-470 at the dose of 60 mg/kg body weight beginning on day nine; group three ( $n=5$ ) received a saline injection. On a clinical 1.5T magnet, the investigators obtained a  $T_1$  map with a variable flip angle 3D GRE approach as described above;  $TR/TE=50\text{ms}/7\text{ms}$ , acquisition matrix =  $88 \times 128$ , FOV = 44 cm x 64 cm, slice thickness=2 mm, flip angles= 2°, 5°, 10°, 15°, 25°, 35°. The dynamic study employed the same acquisition matrix and FOV, but slices were 4 mm thick. The contrast agent was the FDA approved gadopentate dime-glumine (Omniscan). This protocol allowed for 39s temporal resolution and data was collected for 32.5 minutes. An AIF was obtained directly from the aorta (which was in the FOV) signal intensity time course. Analysis was done using the model of Daldrup, *et al*,

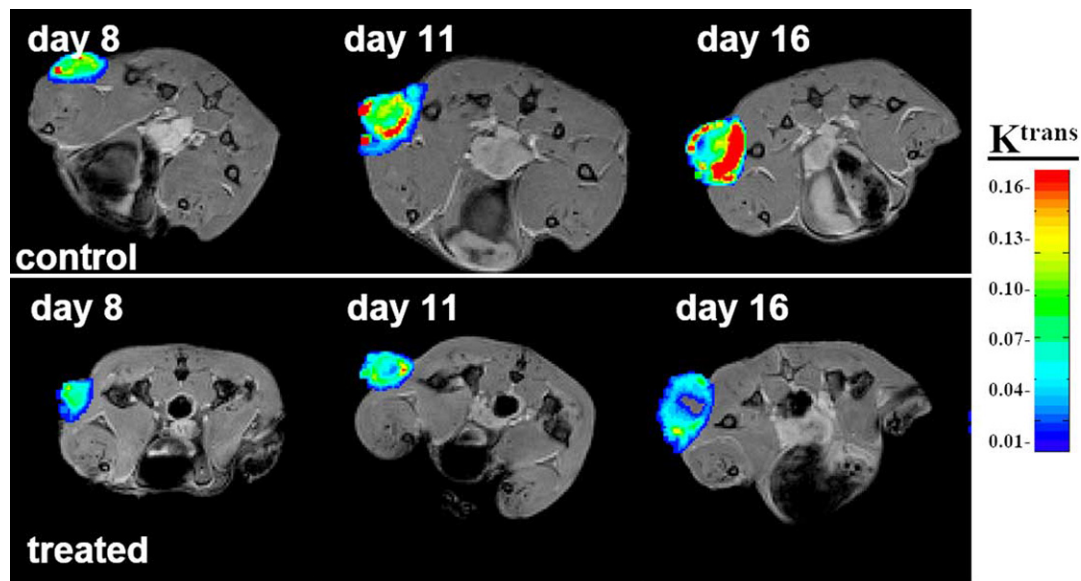


**Fig. (5).** The ability to measure pharmacokinetic parameters as a function of time allows for the potential of characterizing response to treatment. Here 4T1 mammary carcinomas (control and treated by an anti-angiogenic agent) are followed over 16 days by DCE-MRI  $K^{trans}$  maps. By day 16 it is evident that the treated animal has significantly lower  $K^{trans}$  values than the control. This approach not only allows for comparing groups, but also lets each animal serve as its own control.

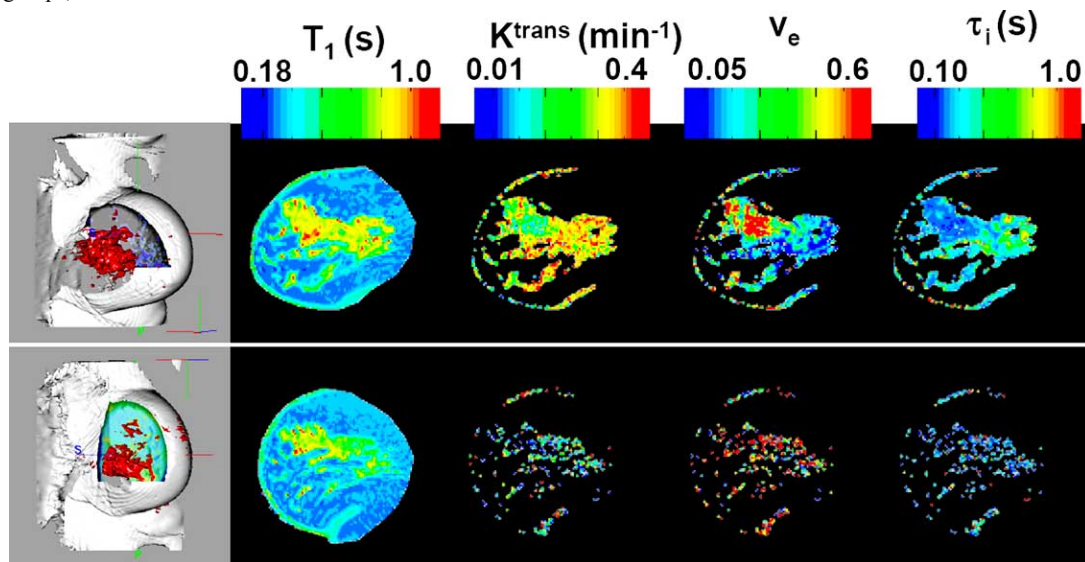


**Fig. (6).** Pre (top row) and post-treatment (bottom row) each parameter's assessment of tumor extent of a representative patient (different from that displayed in figure 2) are presented. (Treatment included four cycles of Taxotere.) The volume on the far left is that obtained from the  $K^{trans}$  parameter and is rendered at 50% of the maximum value obtained from the pre-treatment study. Comparing the top row to the bottom row, the  $T_1$ ,  $K^{trans}$ , and  $v_e$  maps all have a significant drop in parameter values and indicate a tremendous drop in extent of disease.

[90] which is similar to Eq. (12) above returning estimates of  $K^{trans}$ ,  $v_p$  (referred to as  $f^{PV}$  (fractional plasma volume) in this paper), and  $k_{ep}$  ( $= K^{trans}/v_e$ ; though the authors report this value as  $k$ , also a discontinued term). Manually outlined ROI analysis of tumor rim and periphery was performed, as well as voxel-by-voxel analysis. The authors report that both anginex and TNP-470 resulted in smaller tumor volumes and lower mean vessel density ( $P < 0.05$ ) than the saline animals. Anginex and TNP-470 resulted in decreases in  $K^{trans}$  64% ( $P < 0.01$ ) and 44% ( $P < 0.17$ ), respectively. No significant reduction in  $v_p$  or  $k_{ep}$  was found. The authors reported that when mean vessel density maps were aligned and compared to the  $K^{trans}$  maps, both measures showed a statistical

significant increase in values in the tumor rim over the tumor core in the control animals, but not in the saline-treated animals. Correlation between  $K^{trans}$  and microvessel density was not reported. The authors conclude that the effects of these two anti-angiogenic compounds can be assessed with Omniscan on a 1.5T MR scanner.

McIntyre, *et al.*, studied the effects of the vascular-targeted therapy ZD6126 on GH3 prolactinomas in rats [91]. Since the efficacy, dose-response, and short term (~24 hours) effects of this drug have already been studied, the authors investigated the longer term (to 96 hours) effects. ZD6126 is N-acetylcholinol-O-phosphate which has been shown to



induce central necrosis and reduction of tissue blood flow by causing microtubule destabilization in the endothelial cells of tumor-associated neovasculature [92,93]. GH3 prolactinomas were grown in the flanks of Wistar Furth rats ( $n=8$ ) until they reached  $\sim 1.7 \text{ cm}^3$  in size. The animals were then treated with 50mg/kg body weight ZD6126 which has been shown to have a statistically significant effect on tumor necrosis [94]. MR imaging used a multi- $TR$  spin echo approach to obtain the  $T_{10}$  map with  $TE=10$  ms, and  $TR=120, 500, 2000$ , and 10 seconds. The slice thickness was 2 mm,  $FOV=60\text{mm}^2$ , acquisition matrix =  $128^2$ . The dynamic MR protocol also employed a spin-echo sequence with  $TR/TE=120\text{ms}/10\text{ms}$  with a temporal resolution of 15.4 seconds; five images were obtained before and 40 images were obtained after injection of 0.1 mmol/kg Omniscan. This protocol was used to image the animals before treatment and then two animals at each of the following time points: 24, 48, 60, 72, or 96 hours treatment. The authors performed a semi-quantitative analysis returning a value of iAUC for the tumor center and tumor periphery. The iAUC measure was normalized to a reference tissue (muscle) and voxels which had a normalized value greater than 1.0 were defined to be highly enhancing, the “highly enhancing fraction” (HEF) was then computed for each animal at each time point. The investigators state that the HEF can be considered an estimation of the fraction of tumor volume that is well-vascularized [94]. All tumors showed a significant reduction in HEF 24 hours post-treatment (46% reduction,  $P = 0.008$ ), and there was no perfusion recovery even 96 hours post-treatment (median difference 0.004,  $P =$  not significant). The tumor necrosis score (as measured from histology) correlated to HEF for all time points from 48 to 96 hours post-treatment (Kendall  $\tau = -0.714$ ,  $P=0.013$ ). The authors summarize by stating that DCE-MRI allowed for evaluating the longer term effects of ZD6126 in this rat tumor model.

Checkley, *et al.* used DCE-MRI to study the acute effects of vascular permeability and perfusion in PC-3 human prostate adenocarcinoma xenografts following inhibition of vascular endothelial growth factor-A by ZD6474 [95]. The concentration of this growth factor is elevated in tumors and its activity has been shown to be nearly restricted to two high affinity receptors, Flt-1 and KDR/Flk-1 which are expressed on proliferating endothelial cells. ZD6474 is orally active compound that inhibits KDR activity and has been shown to inhibit tumor growth in several animal models [96] and is currently in clinical trials. Swiss athymic mice were injected subcutaneously with  $10^6$  cells on the flank. Tumors were allowed to reach  $\sim 1 \text{ cm}^3$  before they animals were separated into treated and control groups ( $n=11$ ). The treatment groups received 12.5 mg/kg/day ( $n=6$ ), 25 mg/kg/day ( $n=6$ ), 50 mg/kg/day ( $n=10$ ), 100 mg/kg/day ( $n=11$ ). A multi- $TR$  spin echo approach was used to obtain a  $T_{10}$  map with  $TE=10$ , an acquisition matrix of  $512 \times 256 \times 4$  (yielding a spatial resolution of  $0.625 \times 0.312 \times 2 \text{ mm}^3$ ), and  $TR=120, 500, 2000$ , and 10,000 ms. The same parameters as above, but with  $TR=120\text{ms}$ , were employed for the dynamic scans yielding 40 image sets with a temporal resolution of 16 s. MRI was conducted before and after treatment. Data analysis employed the Tofts and Kermode model (similar to Eq. (11); [97]) which returns estimates on  $K^{trans}$  and  $v_e$ . Animals receiving acute doses  $\geq 25$  mg/kg showed a significant

decrease in mean tumor  $K^{trans}$  ( $P=0.04, 0.0005, 0.0004$  for doses of 25, 50 and 100 mg/kg, respectively), and animals receiving doses  $\geq 50$  mg/kg showed a significant decrease in mean tumor  $v_e$  ( $P=0.0001$ , and  $P<0.0001$  for doses of 50 and 100 mg/kg, respectively). The authors conclude that DCE-MRI may allow for assessing changes in vascular characteristics before the anti-angiogenic effects are clinically evident.

SU6668 is an oxindole compound which has been shown to be a selective inhibitor of the angiogenic tyrosine kinases Flk-1/KDR, platelet derived growth factor, and fibroblast growth factor receptors [98,99]. It has been shown to induce apoptosis in both tumor microvessels and in the tumor cells themselves. Marzola, *et al.*, [100] used DCE-MRI and a macromolecular contrast agent (Gd-DTPA-albumin [101, 102]) to measure  $K^{trans}$  and  $v_p$  in a colon carcinoma mouse tumor model. Thirty mice had HT-29 human colon carcinoma fragments implanted subcutaneously on their flanks. Tumors were allowed to grow to the weight of  $\sim 500$  mg and divided into three groups and each group was further divided into 5 controls and 5 treated animals: group one (received one dose of SU6668 (200mg/kg body weight) and was imaged before and 24 h after treatment; group two received SU6668 (same dose) daily for 3 days and was imaged before and 72 h after treatment; group three received SU6668 (same dose) daily for 14 days and was imaged before and on days 7 and 14 after treatment. For the  $T_{10}$  map, a 3D IR-snapshot fast low angle shot protocol was employed with an acquisition matrix of  $128 \times 64 \times 32$  over a  $5 \times 2.5 \times 3 \text{ cm}^3$  FOV (corresponding to a  $0.143 \text{ mm}^3$  voxel size). The dynamic imaging employed a 3D SPGRE sequence with  $TR/TE/\alpha = 50\text{ms}/3.5\text{ms}/90^\circ$  and the same acquisition matrix and FOV which can acquire an image in 104 s. With 30 s intervals in between each image, 24 images were acquired. Both ROI (for tumor rim and core) and voxel analysis was performed with an equation similar to Eq. (12) [101]. In the group one animals, statistically significant reductions in both  $K^{trans}$  and  $v_p$  were seen in the treated sets for the tumor rim ( $P<0.001$ ) and the tumor core ( $P<0.05$ ). For group two, only the  $K^{trans}$  value in the tumor rim showed a significant reduction in the treated versus control set ( $P<0.05$ ). Statistics regarding group three were not reported. The authors conclude that these results should be of interest in the “planning and evaluation of clinical trials for the whole class” of SU6668 compounds.

## 5.2. Clinical Studies

Given the successes that DCE-MRI has achieved in the pre-clinical studies in animal tumor models, it is not surprising that the technique has begun to be applied in human studies. Evelhoch, *et al.* reported on the ability of semi-quantitative analysis of DCE-MRI data to measure the antivascular effects of ZD6126 on both murine and human tumors [103]. Here we discuss only the results of the human studies. ZD6126 is vascular targeting agent that is designed to disrupt the tubulin cytoskeleton of newly formed endothelial cells associated with the process of angiogenesis in the neovasculature of tumors. The study considered patients with a range of (advanced) cancers including carcinomas of the colon, ovary, kidneys, breast, and rectum. Patients were imaged before and 6 h after treatment. The

DCE-MR imaging protocol employed a SPGRE sequence to obtain 16 8 mm slices zero-filled to 32 4mm slices with  $TR/TE = 3.8 \text{ ms}/1.8\text{ms}$ ; each slice was  $128 \times 256$  and zero-filled to  $256 \times 256$ . The iAUC was calculated from the first 60 s of images (approximately the first 8 images). ZD6126 was dosed at levels of  $56 \text{ mg/m}^2$ ,  $80 \text{ mg/m}^2$ , or  $112 \text{ mg/m}^2$ . The investigators showed that, in the post-treatment studies, the iAUC was reduced by 36-72%, with increased doses leading to increased reductions ( $P < 0.05$ ). The authors concluded that DCE-MRI, as quantified by the iAUC, is a useful endpoint for quantifying the antivascular effects of ZD6126 on tumors.

The correlation between microvessel density (MVD) and DCE-MRI parameters in prostate cancer was explored by Schlemmer and colleagues [104]. Twenty-eight patients with biopsy confirmed prostate cancer were included in this study. For the DCE-MRI portion of the study, an inversion recovery turbo fast low-angle shot sequence with  $TR/TE/\alpha = 1300\text{ms}/4.2\text{ms}/13^\circ$ . They acquired ten 4 mm slices in 13 s and acquired 22 consecutive frames. Data analysis employed another variation on the formalism presented above which returns estimates of degree of signal enhancement (the “amplitude”; this parameter depends on the tissues  $T_1$ ,  $T_2$ ,  $K^{trans}$ , and  $v_e$ , as well as imaging parameters) and  $k_{ep}$  (though authors report it as  $k_{21}$ , a name which has since been retired; [20]); this model was first developed by Brix, *et al* [105]. For each patient one histopathological section showing the central and peripheral zones of the tumor was manually paired with the corresponding  $T_2$ -weighted spin echo image and then the  $T_2$ -weighted images were paired to the DCE-MRI slices. DCE-MRI parameters were correlated to MVD measurements by manually outlining ROIs in the tumor and in adjacent normal appearing tissue and performing standard correlation analysis on the respective DCE-MRI parameters and the MVD estimates. In addition to observing significantly elevated values of  $K^{trans}$  in the carcinoma compared with the normal peripheral zone (and no significant difference in the amplitude parameter between the two parameters), the authors report a strong correlation between  $k_{ep}$  and MVD ( $r = 0.80$ ,  $p < 0.001$ ). The authors conclude that DCE-MRI has the potential to provide information on assessing prognosis in prostate cancer patients on an individualized basis.

Stevenson, *et al.* [106] reported on the ability to probe the antivascular effects of combretastatin A4 phosphate using DCE-MRI in a phase I trial. Combretastatin A4 phosphate (CA4P) is a synthetic phosphorylated analog of combretastatin A4 which binds tubulin at the colchicine-binding site and therefore inhibits microtubule polymerization. CA4P is converted to CA4 by phosphatases overexpressed on proliferating endothelial cells. Consequently, CA4P has been shown to selectively induce apoptosis (programmed cell death) in the proliferating endothelial cells which form the neovasculature associated with aggressive tumors [107,108]. The trial consisted of administering CA4P over ten minutes for five consecutive days (in doses of 6 to  $75 \text{ mg/m}^2$ ) to patients with histologically confirmed advanced cancer for which no effective therapy was available. MRI was performed within five days before initiation of treatment and on completion of the day five dose. An

inversion recovery prepared multi-slice fast SPGRE sequence was employed for the  $T_{10}$  map. The dynamic protocol used a 3D fast SPGRE sequence with  $TR/TE/\alpha = 7.8\text{ms}/4.2\text{ms}/30^\circ$  and a  $256 \times 128$  acquisition matrix over a FOV of 36 to 40 cm; 8-18 slices were acquired in 9-18 seconds for and continued for 5-7 minutes. Data analysis employed the model of Tofts and Kermode [97] which is of the kind presented above and returns  $K^{trans}$  and  $v_e$ . Tumor ROIs were manually drawn for each slice containing visible tumor as determined by an experienced MRI radiologist. Of the 37 patients studied with this protocol, the  $52\text{-}65 \text{ mg/m}^2$  was found to be reasonably well-tolerated and antitumor efficacy was observed. Of the ten patients yielding analyzable DCE-MRI data,  $K^{trans}$  was found to decrease in eight. Tumors with the largest baseline enhancement (i.e., before treatment) showed the greatest drop in  $K^{trans}$  after treatment ( $r = -0.89$ ,  $P < 0.001$ ). A significant negative correlation between  $K^{trans}$  and the day 5 CA4 area under the concentration time curve was found ( $r = 0.549$ ,  $p < 0.05$ ).

All of the previous methods relied on analyzing ROI curves to assess tumor characteristics. A potentially more comprehensive assessment of treatment response was presented by Chang, *et al.* who used DCE-MRI to evaluate tumor response over the course of neoadjuvant chemotherapy in 13 patients with locally advanced breast cancer [109]. Data collection employed a 3D fast low angle shot sequence to obtain 30 4-5 mm slices with  $TR/TE/\alpha = 12/3.1 \text{ ms}/25^\circ$ ; each slice was  $176 \times 512$ . Their analysis also employed the formalism presented by Brix, *et al.*, [105] which reports the maximum signal intensity amplitude achieved and the redistribution rate constant  $k_{ep}$  (though the authors define it as “ $k_{out}$ ”). Noting that ROI analysis of one slice of the tumor is by definition not ideal, the authors conducted a voxel-by-voxel analysis to construct parameter histograms which then allowed computation of standard statistical indices: mean, standard deviation, skewness, and kurtosis. To assess the predictive value of these measures, the correlation coefficient ( $r$ ) was computed between these metrics and tumor response (as defined by change in tumor volume) after the each round of therapy. The authors found that histograms associated with responders displayed parameter histograms that showed a decrease and left shift of the peak (towards smaller values), and a narrowing of the base. Kurtosis and standard deviation of amplitude before chemotherapy correlated with tumor response ( $r = 0.63$ ,  $p = 0.03$  and  $0.61$ ,  $p = 0.02$ , respectively). Changes in standard deviation of amplitude correlated with tumor response ( $r = 0.79$ ,  $p = 0.001$ ) after the first course of chemotherapy, as did kurtosis and standard deviation of  $k_{out}$  ( $r = 0.57$ ,  $p = 0.04$  and  $r = 0.57$ ,  $p = 0.04$ , respectively). When comparing the final pre-operative DCE-MRI data with that obtained before treatment, the best tumor response was indicated by a change in amplitude as measured by increased kurtosis ( $r = 0.62$ ,  $p = 0.02$ ), and a decrease in mean ( $r = 0.84$ ,  $p = 0.0003$ ) and standard deviation ( $r = 0.77$ ,  $p = 0.002$ ).

For additional examples of clinical applications of DCE-MRI to cancer (including an example that found DCE-MRI to not be useful technique in evaluating treatment response) the interested reader is referred to references [110-114].

## 6. FUTURE GOALS

In order for a noninvasive, indirect, imaging technique such as DCE-MRI to gain clinical acceptance and realize its full potential, **issues of standardization, repeatability, reproducibility, and validation must be addressed**. Some recent progress has been made in these areas. For example, the National Cancer Institute has encouraged the development and application of DCE-MRI and to develop guidelines for performing quantitative DCE-MRI studies [115]. Additionally, the multi-centre breast screening study in high risk women performed in the UK has gone through great efforts to standardize the protocol for their studies and has published their protocol [116,117]. Cancer Research UK has also published recommendations for using MRI (including DCE-MRI) in early stage clinical trials [118,119]. There have also been recent efforts on defining a standardized reading protocol for DCE-MRI studies [120].

Studies assessing the **repeatability and reproducibility** of various DCE-MRI studies have also been investigated. A **repeatability study is one which aims to assess the closeness of agreement amongst consecutive measurements for the same output value of the input under the same operating conditions**. Thus, a study which employed multiple contrast injections (in close proximity) followed by modeling and comparison of  $K^{trans}$ ,  $v_e$ , iAUC, etc. would be a repeatability study. A **reproducibility study aims to characterize the closeness of output values from the same input value when a period of time has passed (and conditions changed) between consecutive measurements**. Thus, multiple DCE-MRI studies performed with a significant separation in time followed by comparison of output parameters would be a reproducibility study. A series of papers published by the Padhani group in 2002 evaluated the reproducibility of DCE-MRI parameters on both a voxel by voxel and ROI basis in normal human tissues as well as in tumors [121,122] and employed a straightforward methodology which is clearly explained and can serve as an example for all such studies. In this study the authors list changes that would need to be seen in DCE-MRI parameters (both quantitative and semi-quantitative) for a statistically significant change to occur over a range of tissues. The authors concluded by stating “that **reproducibility studies are recommended when treatment effect are being monitored**” [121]. Roberts, *et al.* recently reported on a comparison of robustness of compartmental modeling to model-free analysis and found that the model-based approach is preferred since it provides more insight into physiology without a reduction in power—at a cost in complexity and time [123]. Very recently, Morgan, *et al.* developed and tested a single slice technique that they showed has a coefficient of variation of 19.1 % and 15.8% for  $K^{trans}$  and the iAUC, respectively [124]. There have also been recent efforts aimed at assessing the reproducibility of reference region DCE-MRI models and their comparison to more standard analysis techniques; the interested reader is referred to references [42,125]. The studies described above can be instructive for designing new repeatability/reproducibility studies as well as assessing the degree of change required in a particular model parameter before a significant change can be observed.

Validating the parameters returned from DCE-MRI studies is potentially more difficult as comparison to the gold-standard of histology is quite cumbersome. While there have been a number of studies that compare histology sections to DCE-MRI measures (see, e.g., [126-128]) these have typically been performed with little emphasis on co-localizing the histology sections to the MR “sections”. This is no doubt due to the great discrepancy in spatial scales (microns to millimeters) and the fact that the histology sections are prepared in a way that does not readily retain shape, orientation, or location information. Nonetheless, some very recent progress on this front has been made. Holland, *et al.* presented a method by which high-resolution MR images of breast specimens were correlated with low-resolution microscopic histology and pathology [129]. More recently, Rouviere, *et al.* published a series of papers on employing fiducial markers for correlating *in vivo* animal data to histological sections [130,131] which included a method for cutting specimens along the imaging plane. Efforts to accurately co-register mouse brain MR images to histology sections have also been investigated [132]. These efforts need to be expanded upon to validate (or refute) the DCE-MRI measures as well as to gain clinical acceptance of the techniques.

## 7. CONCLUSION

In this review we discussed the basic requirements for obtaining dynamic contrast enhanced MRI data, the basic theory of several mathematical models for analysis of such data, and how DCE-MRI is being used to assess tumor growth and treatment response in both the pre-clinical and clinical settings. In considering these examples, one particular point deserves special consideration; **the methods for both data acquisition and data analysis are extremely varied from study to study**. If the methods of DCE-MRI are to be applied on a larger scale in the clinic, a directed effort to standardize and assess the robustness of the approach at multiple sites needs to be investigated. This is indeed a difficult task because standardizing a technique requires realistic validation and reproducibility studies, something that the DCE-MRI community has thus far under explored. Thus, while DCE-MRI has the very great ability to probe tumor heterogeneity quantitatively, non-invasively, and at reasonably high-resolution, there remains many barriers to truly bringing it into the arsenal of the practicing clinical oncologist.

## ACKNOWLEDGEMENTS

We thank the National Institutes of Health for funding through NIBIB 1K25 EB005936-01. We thank Dr. P. Charles Lin and Ms. Laura Debusk for providing the mice and treatments depicted in Figs. 3-5. We thank our colleagues Drs. Martin Lepage, Anuradha Chakravarthy, Kenneth J. Niernann, Mark C. Kelley, Ingrid Meszoely, and Ingrid A. Mayer. Dr. Jeffrey J. Luci for many helpful and informative conversations.

## REFERENCES

- [1] Ribatti D, Vacca A, Presta M. The discovery of angiogenic factors: a historical review. *Gen Pharmacol* 2000; 35: 227-31
- [2] Folkman J. Role of angiogenesis in tumor growth and metastasis. *Semin Oncol* 2002; 29(6 Suppl 16): 15-8.



- [3] Folkman J. Angiogenesis in cancer, vascular, rheumatoid and other disease. *Nat Med* 1995; 1: 27-31
- [4] Atri M. New Technologies and Directed Agents for Applications of Cancer Imaging. *J Clin Onc* 2006; 24: 3299-3308
- [5] Carmeliet P and Jain RK. Angiogenesis in cancer and other diseases. *Nature* 2000; 407: 249-57.
- [6] Verhoef C, de Wilt JH, Verheul HM. Angiogenesis inhibitors: perspectives for medical, surgical and radiation oncology. *Curr Pharm Des*. 2006; 12: 2623-30.
- [7] Gillies RJ, Bhujwala ZM, Evelhoch J, *et al.* Applications of magnetic resonance in model systems: tumor biology and physiology. *Neoplasia* 2000; 2: 139-51.
- [8] Evelhoch JL, Gillies RJ, Karczmar GS, *et al.* Applications of magnetic resonance in model systems: cancer therapeutics. *Neoplasia* 2000; 2: 152-165.
- [9] Caravan P, Ellison JJ, McMurry TJ, Lauffer RB. Gadolinium(III) chelates as MRI contrast agents: structure, dynamics, and applications. *Chem Rev* 1999; 99: 2293-2352.
- [10] Bushberg JT, Seibert JA, Leidholdt EM, Boone JM. The essential physics of medical imaging, second edition. Lippincott Williams, and Wilkins, Philadelphia; 2002.
- [11] Hendee WR, Ritenour ER. Medical Imaging Physics, fourth edition. Wiley-Liss, New York; 2002.
- [12] Cho Z-H, Jones JP, Singh M. Foundations of medical imaging. John Wiley and sons, New York; 1993.
- [13] Haacke EM, Brown RW, Thompson MR, Venkatesan R. Magnetic Resonance Imaging: Physical Principles and Sequence Design. Wiley-Liss, New York; 1999.
- [14] Abragam A. Principles of Nuclear Magnetism. Clarendon Press, Oxford; 1961.
- [15] Callaghan PT. Principles of nuclear magnetic resonance microscopy. Clarendon Press, Oxford; 1991.
- [16] deGraad R. *In vivo* NMR spectroscopy: principles and techniques. John Wiley and Sons, New York; 1999.
- [17] Lauffer RB. Paramagnetic metal complexes as water proton relaxation agents for NMR imaging: theory and design. *Chem Rev* 1987; 87: 901-927.
- [18] Stanis GJ, Henkelman RM. Gd-DTPA relaxivity depends on macromolecular content. *Magn Reson Med* 2000; 44: 665-7.
- [19] Donahue KM, Burstein D, Manning WJ, Gray ML. Studies of Gd-DTPA relaxivity and proton exchange rates in tissue. *Magn Reson Med* 1994; 32: 66-76.
- [20] Tofts PS, Brix G, Buckley DL, *et al.* Estimating kinetic parameters from dynamic contrast-enhanced T<sub>1</sub>-weighted MRI of a diffusible tracer: Standardized quantities and symbols. *J Magn Reson Imaging* 1999; 10: 223-232.
- [21] Cron GO, Santyr G, Kelcz F. Accurate and rapid quantitative dynamic contrast-enhanced breast MR imaging using spoiled gradient-recalled echoes and bookend T<sub>1</sub> measurements. *Magn Reson Med* 1999; 42: 746-753.
- [22] Cron GO, Kelcz F, Santyr GE. Improvement in breast lesion characterization with dynamic contrast-enhanced MRI using pharmacokinetic modeling and bookend T<sub>1</sub> measurements. *Magn Reson Med*, 2004; 51: 1066-1070.
- [23] Roberts C, Issa B, Stone A, Jackson A, Waterton JC, Parker GJM. Comparative study into the robustness of compartmental modeling and model-free analysis in DCE-MRI studies. *J Magn Reson Imaging* 2006; 23: 554-563.
- [24] Harrer JU, Parker GJM, Haroon HA, *et al.* Comparative study of methods for determining vascular permeability and blood volume in human gliomas. *J Magn Reson Imaging* 2004; 20: 748-757.
- [25] Parker GJ, Roberts C, Macdonald A, *et al.* Experimentally-derived functional form for a population-averaged high-temporal-resolution arterial input function for dynamic contrast-enhanced MRI. *Magn Reson Med* 2006; 56: 993-1000.
- [26] Gossman A, Helbich TH, Kuriyama N, *et al.* Dynamic contrast-enhanced magnetic resonance imaging as a surrogate marker of tumor response to anti-angiogenic therapy in a xenograft model of glioblastoma multiforme. *J Magn Reson Imaging* 2002; 15: 233-40.
- [27] Noworolski SM, Henry RG, Vigneron DB, Kurhanewicz J. Dynamic contrast-enhanced MRI in normal and abnormal prostate tissues as defined by biopsy, MRI, and 3D MRSI. *Magn Reson Med* 2005; 53: 249-255.
- [28] Parker GJ, Barker GJ, Tofts PS. Accurate multislice gradient echo T(1) measurement in the presence of non-ideal RF pulse shape and RF field nonuniformity. *Magn Reson Med*. 2001; 45: 838-45.
- [29] Deichmann R. Fast high-resolution T<sub>1</sub> mapping of the human brain. *Magn Reson Med* 2005; 54: 20-7
- [30] Henderson E, McKinnon G, Lee TY, Rutt BK. A fast 3D look-locker method for volumetric T<sub>1</sub> mapping. *Magn Reson Imaging* 1999; 17: 1163-71.
- [31] Zhu DC, Penn RD. Full-brain T<sub>1</sub> mapping through inversion recovery fast spin echo imaging with time-efficient slice ordering. *Magn Reson Med* 2005; 54(3): 725-31.
- [32] Furman-Haran E, Grobgedl D, Kelcz F, Degani H. Critical role of spatial resolution in dynamic contrast-enhanced breast MRI. *J Magn Reson Imaging* 2001; 13: 862-7.
- [33] Henderson E, Rutt BK, Lee TY. Temporal sampling requirements for the tracer kinetics modeling of breast disease. *Magn Reson Imaging* 1998; 16: 1057-73
- [34] Fritz-Hansen T, Rostrup E, Larsson HBW, Sondergaard L, Ring P, Henrikson O. Measurement of the arterial concentration of Gd-DTPA using MRI: a step toward quantitative perfusion imaging. *Magn Reson Med* 1996; 36: 225-231.
- [35] Larsson HBW, Stubgaard M, Frederiksen JL, Jensen M, Henriksen O, Paulson OB. Quantitation of blood-brain barrier defect by magnetic resonance imaging and Gadolinium-DTPA in patients with multiple sclerosis and brain tumors. *Magn Reson Med* 1990; 16: 117-131.
- [36] Weinmann HJ, Laniado M, Mutzel W. Pharmacokinetics of GdDTPA/Dimeglumine after intravenous injection into healthy volunteers. *Physiol Chem Phys* 1984; 16: 167-172.
- [37] Simpson NE, He Z, Evelhoch JL. Deuterium NMR tissue perfusion measurements using the tracer uptake approach: I. optimization of methods. *Magn Reson Med* 1999; 42: 42-52.
- [38] Kety SS. Peripheral blood flow measurement. *Pharmacol Rev* 1951; 3: 1-41.
- [39] Port RE, KnoppMV, Hoffmann U, Milker-Zabel S, Brix G. Multicompartment analysis of gadolinium chelate kinetics: blood-tissue exchange in mammary tumors as monitored by dynamic MR imaging. *J Magn Reson Imaging* 1999; 10: 233-241.
- [40] van Osch MJO, Vonken E-J PA, Viergever MA, Grond J, Bakker CJG. Measuring the arterial input function with gradient echo sequences. *Magn Reson Med* 2003; 49: 1067-1076.
- [41] McIntyre DJO, Ludwig C, Pasan A, Griffiths JR. A method for interleaved acquisition of a vascular input function for dynamic contrast-enhanced MRI in experimental rat tumours. *NMR in biomedicine*, 2004; 17: 132-143.
- [42] Yankeelov TE, Cron GO, Addison C, *et al.* Comparison of a Reference Region Model to Direct Measurement of an AIF in the Analysis of DCE-MRI Data. *Magn Reson Med*, in press.
- [43] Kim YR, Rebro KJ, Schmainda KM. Water exchange and inflow affect the accuracy of T1-GRE blood volume measurements: implications for the evaluation of tumor angiogenesis. *Magn Reson Med* 2002; 47: 1110-1120.
- [44] Kovar DA, Lewis M, Karczmar GS. A new method for imaging perfusion and contrast extraction fraction: input functions derived from reference tissues. *J Magn Reson Imaging* 1998; 8: 1126-1134.
- [45] Yankeelov TE, Luci JJ, Lepage M, *et al.* Quantitative pharmacokinetic analysis of DCE-MRI data without an arterial input function: a reference region model. *Magn Reson Imag* 2005; 23: 519-529.
- [46] Yang C, Karczmar GS, Medved M, Stadler WM. Estimating the arterial input function using two reference tissues in dynamic contrast-enhanced MRI studies: fundamental concepts and simulations. *Magn Reson Med* 2004; 52: 1110-7.
- [47] Lammertsma AA, Bench CJ, Hume SP, *et al.* Comparison of methods for analysis of clinical [<sup>11</sup>C]Raclopride studies. *J Cereb Blood Flow Metab* 1995; 16: 42-52.
- [48] Taylor JS, Tofts PS, Port R, *et al.* MR imaging of tumor microcirculation: promise for the new millennium. *J Magn Reson Imag* 1999; 10: 903-907.
- [49] Shellock FG, Kanal E. Safety of magnetic resonance imaging contrast agents. *J Magn Reson Imaging* 1999; 10: 477-484.
- [50] Rainville ED, Bedient PE. Elementary Differential Equations. NewYork McMillan; 1989: 139-151.
- [51] Lyng H, Dahle GA, Kaalhus O, Skretting A, Rofstad EK. Measurement of perfusion rate in human melanoma xenografts by contrast-enhanced magnetic resonance imaging. *Magn Reson Med* 1998; 40: 89-98.

- [52] Donahue KM, Weiskoff RM, Parmelee DJ, *et al.* Dynamic Gd-DTPA enhanced MRI measurement of tissue cell volume fraction. *Magn Reson Med* 1995; 34: 423-432.
- [53] Shames D, Kuwatsuru R, Vexler V, Muhler A, Brasch RC. Measurement of capillary permeability to macromolecules by dynamic magnetic resonance imaging: a quantitative non-invasive technique. *Magn Reson Med* 1993; 29: 616-622.
- [54] Preda A, Wielopolski PA, ten Hagen TLM, *et al.* Dynamic contrast-enhanced MRI using macromolecular contrast media for monitoring the response to isolated limb perfusion in experimental soft-tissue sarcomas *MAGMA* 2004; 17: 296-302.
- [55] Lawrence KS, Lee T-Y. An adiabatic approximation to the tissue homogeneity model for water exchange in brain: I. Theoretical derivation. *J Cereb Blood Flow Metab* 1998; 18: 1365-1377.
- [56] Koh TS, Cheong LH, Hou Z, Soh, YC. A physiologic model of capillary-tissue exchange for dynamic contrast-enhanced imaging of tumor microcirculation. *IEEE Trans Biomed Eng* 2003; 50: 159-167.
- [57] Moran GR, Prato FS. Modeling tissue contrast agent concentration: A solution to the tissue homogeneity model using a simulated arterial input function. *Magn Reson Med* 2001; 45: 42-54.
- [58] Kuikka JT. Modeling tissue contrast agent concentration: A solution to the tissue homogeneity model using a simulated arterial input function. *Magn Reson Med* 2001; 46: 837.
- [59] Buckley DL. Uncertainty in the analysis of tracer kinetics using dynamic contrast-enhanced  $T_1$ -weighted MRI. *Magn Reson Med* 2002; 47: 601-6.
- [60] Henderson E, Sykes J, Drost D, Weinmann H-J, Rutt BK, Lee T-Y. Simultaneous MRI measurements of blood flow, blood volume, and capillary permeability in mammary tumors using two different contrast agents. *J Magn Reson Imaging* 2000; 12: 991-1003.
- [61] Landis CS, Li X, Telang FW, *et al.* Determination of the MRI contrast agent concentration time course *in vivo* following bolus injection: Effect of equilibrium transcytolemmal water exchange. *Magn Reson Med* 2000; 44: 563-574.
- [62] Landis CS, Li X, Telang FW, *et al.* Equilibrium transcytolemmal water-exchange kinetics in skeletal muscle *in vivo*. *Magn Reson Med* 1999; 42: 467-478.
- [63] McConnell HM. Reaction Rates by Nuclear Magnetic Resonance. *J Chem Phys* 1958; 28: 430-431.
- [64] Woessner DE. Nuclear Transfer Effects in Nuclear Magnetic Resonance Pulse Experiments. *J Chem Phys* 1961; 35: 41-48.
- [65] Lee J. Magnetic resonance studies of tissue  $^{23}\text{Na}$  and  $^1\text{H}_2\text{O}$  signals. Ph.D. Dissertation 1993; State University of New York; Stony Brook, New York. p. 180-186.
- [66] Donahue KM, Weisskoff RM, Chesler DA, *et al.* Improving MR quantification of regional blood volume with intravascular  $T_1$  contrast agents: Accuracy, precision, and water exchange. *Magn Reson Med* 1996; 36: 858-867.
- [67] Schwarzbauer C, Morrissey SP, Deichmann R, *et al.* Quantitative magnetic resonance imaging of capillary water permeability and regional blood volume with an intravascular MR contrast agent. *Magn Reson Med* 1997; 37: 769-777.
- [68] Parkes LM, Tofts PS. Improved accuracy of human cerebral blood perfusion measurements using arterial spin labeling: accounting for capillary water permeability. *Magn Reson Med* 2002; 48: 27-41.
- [69] Cao Y, Brown SL, Knight RA, Fenstermacher JD, Ewing JR. Effect of intravascular-to-extravascular water exchange on the determination of blood-to-tissue transfer constant by magnetic resonance imaging. *Magn Reson Med* 2005; 53: 282-93.
- [70] Yankeelov TE, Rooney WD, Xin Li, Springer CS. Variation of the Relaxographic "Shutter-Speed" for Transcytolemmal Water Exchange Affects CR Bolus-Tracking Curve Shape. *Magn Reson Med* 2003; 50: 1151-1169.
- [71] Yankeelov TE, Rooney WD, Huang W, *et al.* Evidence for Shutter-speed variation in CR bolus-tracking studies of human pathology. *NMR in Biomed* 2005; 18: 173-185.
- [72] Yankeelov TE, Lepage M, Chakravarthy A, *et al.* Integration of Quantitative DCE-MRI and ADC Mapping to Monitor Treatment Response in Human Breast Cancer: Initial Results. *Magn Reson Imag* in press.
- [73] Li X, Huang W, Yankeelov TE, Tudorica A, Rooney WD, Springer CS. Shutter-Speed Analysis of CR Bolus-Tracking Data Facilitates Discrimination of Benign and Malignant Breast Disease. *Magn Reson Med* 2005; 53: 724-9.
- [74] Zhou R, Pickup S, Yankeelov TE, Springer CS, Glickson JD. Simultaneous measurement of arterial input function and tumor pharmacokinetic in mice by dynamic contrast enhanced imaging: effects of equilibrium transcytolemmal water exchange. *Magn Reson Med* 2004; 52: 248-257.
- [75] Li X, Rooney WD, Springer CS Jr. A unified magnetic resonance imaging pharmacokinetic theory: intravascular and extracellular contrast reagents. *Magn Reson Med* 2005; 54(6): 1351-9.
- [76] Jesberger JA, Rafie N, Duerk JL, Sunshine JL, Mendez M, Remick SC, Lewin JS. Model-free parameters from dynamic contrast-enhanced-MRI: sensitivity to EES volume fraction and bolus timing. *J Magn Reson Imaging* 2006; 24: 586-94.
- [77] Walker-Samuel S, Leach MO, Collins DJ. Evaluation of response to treatment using DCE-MRI: the relationship between initial area under the gadolinium curve (IAUGC) and quantitative pharmacokinetic analysis. *Phy Med Bio* 2006; 51: 3593-602.
- [78] Daniel BL, Yen YF, Glover GH, *et al.* Breast disease: dynamic spiral MR imaging. *Radiology* 1998; 209(2): 499-509.
- [79] Mussurakis S, Gibbs P, Horsman A. Primary breast abnormalities: selective pixel sampling on dynamic gadolinium-enhanced MR images. *Radiology* 1998; 206: 465-73.
- [80] Rieber A, Brambs HJ, Gabelmann A, Heilmann V, Kreienberg R, Kuhn T. Breast MRI for monitoring response of primary breast cancer to neo-adjuvant chemotherapy. *Eur Radiol* 2002; 12: 1711-9.
- [81] Chen W, Giger ML, Lan L, Bick U. Computerized interpretation of breast MRI: Investigation of enhancement-variance dynamics. *Med Phys* 2004; 31: 1076-82.
- [82] Schmid VJ, Whitcher BJ, Yang GZ, Taylor NJ, Padhani AR. Statistical analysis of pharmacokinetic models in dynamic contrast-enhanced magnetic resonance imaging. *Med Image Comput Assist Interv Int Conf Med Image Comput Comput Assist Interv* 2005; 8: 886-93.
- [83] Chen W, Giger ML, Bick U, Newstead GM. Automatic identification and classification of characteristic kinetic curves of breast lesions on DCE-MRI. *Med Phys* 2006; 33: 2878-87.
- [84] Twellman T, Lichte O, Nattkemper TW. An adaptive tissue characterization network for model-free visualization of dynamic contrast-enhanced magnetic resonance image data. *IEEE Trans Med Imaging* 2005; 24: 1256-66.
- [85] Yankeelov TE, Lepage M, Chakravarthy A, *et al.* Integration of Quantitative DCE-MRI and ADC Mapping to Monitor Treatment Response in Human Breast Cancer: Initial Results. *Magn Reson Imag* 2007; 25: 1-13.
- [86] de Lussanet QG, Beets-Tan RGH, Backes WH, *et al.* Dynamic contrast-enhanced magnetic resonance imaging at 1.5 Tesla with gadopentetate dimeglumine to assess the angiostatic effects of anginex in mice. *E J Cancer* 2004; 40: 1262-1268.
- [87] Griffioen AW, van der Schaft DW, Barendsz-Janson AF, *et al.* Anginex, a designed peptide that inhibits angiogenesis. *Biochem J* 2001; 354: 233-242.
- [88] Dings RP, Yokoyama Y, Ramakrishnan S, Griffioen AW, Mayo KH. The designed angiostatic peptide anginex synergistically improves chemotherapy and antiangiogenesis therapy with angiostatin. *Cancer Res* 2003; 63: 382-385.
- [89] Huang J, Frischer JS, New T, *et al.* TNP-470 promotes initial vascular sprouting in xenograft tumors. *Mol Cancer Ther* 2004; 3: 335-343.
- [90] Daldrup H, Shames DM, Wendland M, *et al.* Correlation of dynamic contrast-enhanced MR imaging with histologic tumor grade: comparison of macromolecular and small-molecular contrast media *Am J Roentgenol* 1998; 171: 941-949.
- [91] McIntyre DJO, Robinson SP, Howe FA, *et al.* Single Dose of the Antivascular Agent, ZD6126 (*N*-Acetylcolchicinol-*O*-Phosphate), Reduces Perfusion for at Least 96 Hours in the GH3 Prolactinoma Rat Tumor Model. *Neoplasia* 2004; 6: 150-157.
- [92] Blakely DC, Westwood FR, Walker M, *et al.* Antitumor activity of the novel vascular targeting agent ZD6126 in a panel of tumor models. *Clin Cancer Res* 2002; 8: 1974-1983.
- [93] Davis PD, Dougherty GJ, Blakey DC, *et al.* ZD6126: a novel vascular targeting agent that causes selective destruction of tumor vasculature. *Cancer Res* 2002; 62: 7247-7253.
- [94] Robinson SP, McIntyre DJO, Checkley D, *et al.* Tumor does response to the antivascular agent ZD6126 assessed by magnetic resonance imaging. *Br J Cancer* 2003; 88: 1592-1597.

- [95] Checkley D, Tessier JJ, Kendrew J, Waterton JC, Wedge SR. Use of dynamic contrast-enhanced MRI to evaluate acute treatment with ZD6474, a VEGF signaling inhibitor, in PC-3 prostate tumours *Br J Cancer* 2003; 89: 1889-1895.
- [96] Wedge SR, Ogilvie DJ, Dukes M, *et al.* ZD6474 inhibits vascular endothelial growth factor signaling, angiogenesis, and tumor growth following oral administration. *Cancer Res* 2002; 62(16): 4645-55.
- [97] Tofts PS, Kermode AG. Measurement of the blood-brain barrier permeability and leakage space using dynamic MR imaging. 1. Fundamental concepts. *Magn Reson Med* 1991; 17: 357-367.
- [98] Laird AD, Vajkoczy P, Shawyer LK, *et al.* SU6668 is a potent antiangiogenic and antitumor agent that induces regression of established tumors. *Cancer Res* 2000; 60: 4152-4160.
- [99] Laird AD, Christensen JG, Li G, *et al.* SU6668 inhibits Flk-1/KDR and PDGFR $\beta$  *in vivo*, resulting in rapid apoptosis of tumor vasculature and tumor regression in mice. *FASEB J* 2002; 16: 681-690.
- [100] Marzola P, Degrossi A, Calderan L, *et al.* *In Vivo* Assessment of Antiangiogenic Activity of SU6668 in an Experimental Colon Carcinoma Model. *Clin Can Res* 2004; 10: 739-750.
- [101] Daldrup H, Shames DM, Wendland M, *et al.* Correlation of dynamic contrast-enhanced magnetic resonance imaging with histologic tumor grade: comparison of macromolecular and small-molecular contrast media. *Pediatr Radiol* 1998; 28: 67-78.
- [102] Brasch R, Turetschek K. MRI characterization of tumors and grading angiogenesis using macromolecular contrast media: status report. *E J Radiol* 2000; 34: 148-155.
- [103] Evelhoch JL, LoRusso PM, He Z, *et al.* Magnetic Resonance Imaging Measurements of the Response of Murine and Human Tumors to the Vascular-Targeting Agent ZD6126. *Clin Can Res* 2004; 10: 3650-3657.
- [104] Schlemmer H-P, Merkle J, Grobholz R, *et al.* Can pre-operative contrast-enhanced dynamic MR imaging for prostate cancer predict microvessel density in prostatectomy specimens? *Eur Radiol* 2004; 14: 309-317.
- [105] Brix G, Semmler W, Port R, Schad LR, Leyer G, Lorenz WJ. Pharmacokinetic parameters in CNS Gd-DTPA enhanced MR imaging. *J Comput Assist Tomogr* 1991; 15: 621-628.
- [106] Stevenson JP, Rosen M, Sun W, *et al.* Phase I Trial of the Antivascular Agent Combretastatin A4 Phosphate on a 5-Day Schedule to Patients With Cancer: Magnetic Resonance Imaging Evidence for Altered Tumor Blood Flow. *J Clin Oncol* 2003; 21: 4428-4438.
- [107] Iyer S, Chaplin DJ, Rosenthal DS, *et al.* Induction of apoptosis in proliferating human endothelial cells by the tumor-specific antiangiogenesis agent combretastatin A-4. *Cancer Res* 1998; 58: 4510-4514.
- [108] Grosios K, Holwell SE, McGown AT, *et al.* *In vivo* and *in vitro* evaluation of combretastatin A-4 and its sodium phosphate prodrug. *Br J Cancer* 1999; 81: 1318-1327.
- [109] Chang Y-C, Huang C-S, Liu Y-J, Chen J-H, Lu Y-S, Tseng W-YI. Angiogenic response of locally advanced breast cancer to neoadjuvant chemotherapy evaluated with parametric histogram from dynamic contrast-enhanced MRI. *Phy Med Bio* 2004; 49: 3593-3602.
- [110] Giesel FL, Bischoff H, von Tengg-Koblighk H, *et al.* Dynamic contrast-enhanced MRI of malignant pleural mesothelioma: a feasibility study of noninvasive assessment, therapeutic follow-up, and possible predictor of improved outcome. *Chest* 2006; 129: 1570-6.
- [111] Hawighorst H, Knopp MV, Debus J, *et al.* Pharmacokinetic MRI for assessment of malignant glioma response to stereotactic radiotherapy: initial results. *J Magn Reson Imaging* 1998; 8: 783-8.
- [112] Atkin G, Taylor NJ, Daley FM, *et al.* Dynamic contrast-enhanced magnetic resonance imaging is a poor measure of rectal cancer angiogenesis. *Br J Surg* 2006; 93: 992-1000.
- [113] Khiat A, Gianfelice D, Amara M, Boulanger Y. Influence of post-treatment delay on the evaluation of the response to focused ultrasound surgery of breast cancer by dynamic contrast enhanced MRI. *Br J Radiol* 2006; 79: 308-14.
- [114] Wedam SB, Low JA, Yang SX, *et al.* Antiangiogenic and antitumor effects of bevacizumab in patients with inflammatory and locally advanced breast cancer. *J Clin Oncol* 2006; 24: 769-77.
- [115] Evelhoch J, Garwood M, Vigneron D, *et al.* Expanding the Use of Magnetic Resonance in the Assessment of Tumor Response to Therapy: Workshop Report. *Cancer Res* 2005; 65: 7041-4.
- [116] Brown J, Coulthard A, Dixon AK, *et al.* Protocol for a national multi-centre study of magnetic resonance imaging screening in women at genetic risk of breast cancer. *The Breast*, 2000; 9: 78-82.
- [117] Brown J, Buckley D, Coulthard A, *et al.* *Magn Reson Imaging* 2000; 18: 765-76.
- [118] Leach MO, Brindle KM, Evelhoch JL, *et al.* Assessment of antiangiogenic and antivascular therapeutics using MRI: recommendations for appropriate methodology for clinical trials. *Br J radiology* 2003; 76: 1: 87-91.
- [119] Leach MO, Brindle KM, Evelhoch JL, *et al.* The assessment of antiangiogenic and antivascular therapies in early-stage clinical trials using magnetic resonance imaging: issues and recommendations. *Br J Cancer* 2005; 9: 1599-610.
- [120] Warren RML, Pointon L, Thompson D, *et al.* Reading Protocol for Dynamic Contrast-enhanced MR Images of the Breast: Sensitivity and Specificity Analysis. *Radiology* 2005; 236: 779-88.
- [121] Galbraith SM, Lodge MA, Taylor NJ, *et al.* Reproducibility of dynamic contrast-enhanced MRI in human muscle and tumours: comparison of quantitative and semi-quantitative analysis. *NMR Biomed* 2002; 15: 132-42.
- [122] Padhani AR, Hayes C, Landau S, Leach MO. Repeatability of quantitative dynamic MRI of normal human tissues. *NMR in Biomedicine* 2005; 15: 143-153.
- [123] Roberts C, Issa B, Stone A, Jackson A, Waterton JC, Parker GJ. Comparative study into the robustness of compartmental modeling and model-free analysis in DCE-MRI studies. *J Magn Reson Imaging* 2006; 23: 554-63.
- [124] Morgan B, Utting F, Higginson A, Thomas AL, Steward WP, Horsfield MA. A simple, reproducible method for monitoring the treatment of tumours using dynamic contrast-enhanced MR imaging. *Br J cancer* 2006; 94: 1420-7.
- [125] Yankeelov TE, Debusk L, Luci JJ, Lin C, Price RR, Gore JC. Repeatability of a Reference Region Model for the Analysis of Murine DCE-MRI Data at 7T. *J Magn Reson Imag*, 2006 in press.
- [126] Tuncbilek N, Karakas HM, Altaner S. Dynamic MRI in indirect estimation of microvessel density, histologic grade, and prognosis in colorectal adenocarcinomas. *Abdom Imaging* 2004; 29: 166-72.
- [127] Wang B, Gao ZQ, Yan X. Correlative study of angiogenesis and dynamic contrast-enhanced magnetic resonance imaging features of hepatocellular carcinoma. *Acta Radiol* 2005; 46: 353-8.
- [128] Su MY, Cheung YC, Fruehauf JP, *et al.* Correlation of dynamic contrast enhancement MRI parameters with microvessel density and VEGF for assessment of angiogenesis in breast cancer. *J Magn Reson Imaging* 2003; 18: 467-77.
- [129] Holland AE, Hendrick RE, Jin H, Russ PD, Barentsz JO, Holland R. Correlation of high-resolution breast MR imaging with histopathology; validation of a technique. *J Magn Reson Imaging* 2000; 11: 601-6.
- [130] Rouvière O, Reynolds C, Hulshizer T, *et al.* Fiducial markers for MR histological correlation in ex vivo or short-term *in vivo* animal experiments: A screening study. *J Magn Reson Imaging* 2006; 23: 50-59.
- [131] Rouvière, MR histological correlation: A method for cutting specimens along the imaging plane in animal or ex vivo experiments. *J Magn Reson Imaging* 2006; 23: 60-69.
- [132] Li X, Yankeelov TE, Rosen G, Gore JC, Dawant BM. Multimodal inter-subject registration of mouse brain images. 2006 *Proc SPIE* 6144; 61440T.